6

APPLICATIONS OF THE CONJUGATE GRADIENT FFT METHOD TO RADIATION AND SCATTERING

J. L. Volakis and K. Barkeshli

6.1 Introduction

The Conjugate Gradient method (CG) is a nonlinear semi-direct iterative scheme for the solution of a system of equations. From its introduction by Hesteness and Steifel [1,2,3], nearly forty years ago, it has been of considerable interest to mathematicians and engineers primarily because in the absence of round-off errors, it ensures convergence in a finite number of steps. In short, convergence is accomplished via a systematic orthogonalization of the solution vector with respect to the residual vector defined as the difference between the left and right hand sides of the system at the end of each iteration. That is, for an N-dimensional system, the solution vector is constructed from a set of N linearly independent (mutually conjugate) vectors orthogonal to the residual vectors. Since these also form a linearly independent set, the exact solution is obtained at the N-th iteration, but in general the solution can be constructed, rather accurately, with only a few of the orthogonal vectors that span the solution space. As a result, convergence is achieved after a subset of N iterations have been completed.

The guaranteed convergence achieved with the conjugate gradient solution method is, of course, a prerequisite for applications to general configurations of interest. However, a primary reason for considering such a solution method is the memory savings which can be realized when the conjugate gradient method is combined with the fast Fourier transform (FFT) [4]. In electromagnetics, a solution of an integro-differential equation is often required for the unknown current density distributions. Typically, these involve convolution integrals whose discrete representation results in a matrix operator demanding a memory storage of $O(N^2)$, where N is the number of unknown coefficients in the assumed current density expansion. For large scale simulations, such a memory demand results in prohibitive storage requirements and, thus, traditional matrix inversion and iterative approaches are not attractive.

However, for a given/assumed current distribution, as is the case with iterative solution methods, the convolution integral can be evaluated without a need to generate the square impedance matrix [5-14]. Instead, the evaluation involves simple algebraic operations on the transforms of the convolved quantities which usually are the current density and the pertinent Green's function. More importantly, the entire evaluation process has an $O(N)$ memory requirement and is, therefore, suited for large scale simulations. An additional feature

of the combined CG and FFT formulation is, of course, the simplicity of the solution process. This is not, generally, shared with other approaches requiring an explicit computation of all elements comprising the matrix operator. Further, while the large condition number of singular operators may result in the failure of a matrix inversion approach to yield an accurate solution, when employing the conjugate gradient method this situation often translates to more iterations before reaching convergence.

A drawback of the iterative solution methods versus direct matrix inversion techniques is their inherent characteristic that the solution process be repeated for all excitations. In scattering computation, where the computation of backscatter patterns is of interest, this makes the iterative solution methods computationally intensive. However, for a single excitation the CG method is generally much faster than matrix inversion techniques, requiring only $4N(1+\log_2 N)$ operations per iteration vs. $O(N^3)$ required with a solution via Gaussian elimination or LU decomposition.

In this chapter, the combined CG and FFT (to be referred hereon as CGFFT) method is employed for the solution of various integral equations arising in radiation and scattering problems. Applications to one, two and three dimensional examples are discussed, including

(1) Radiation from thin wire dipoles

(2) Scattering by dielectric and resistive strips

(3) Scattering by two dimensional composite structures

(4) Radiation of a dipole in the presence of a flat plate

(5) Scattering by perfectly conducting and composite plates

(6) Scattering by coated perfectly conducting plates

and

(7) Scattering by a two dimensional filled groove in a ground plane.

For each application, the pertinent integral equations are derived and placed in a form suitable for a solution via the CGFFT method. A major portion of the presentation deals with issues relating to the discretization of the resulting continuous system. Of particular concern is the introduction of techniques leading to more accurate and efficient formulations. In most cases numerical data are included which validate the methodology and can also serve for future reference. Some of the included results are normally out of the reach of matrix inversion techniques.

6.2 The CGFFT Formulation

The integrodifferential equations considered in this chapter will be of the general form

$$\overline{E}^i(\overline{r}) = \overline{\overline{\eta}}(r) \cdot \overline{J}(\overline{r}) + \iiint_V \overline{\overline{\Gamma}}(|\overline{r} - \overline{r}'|) \cdot \overline{J}(\overline{r}')\, dv' \tag{6.1a}$$

or

$$\overline{E}^i(\overline{r}) = A[\overline{J}] \tag{6.1b}$$

where $\overline{E}^i$ denotes the excitation field, $\overline{J}$ is the unknown current density vector, $\overline{\overline{\Gamma}}$ is the associated dyadic Green's function, $\overline{r}$ and $\overline{r}'$ specify the observation and integration points and $\overline{\overline{\eta}}$ is some given tensor specific to the geometry and electrical properties of the scatterer or radiator. The integral to the right represents the convolution of the current density with the Green's function and can, therefore, be evaluated in the spectral domain by invoking the convolution theorem. Defining the forward and inverse Fourier transform pairs for a one dimensional distribution as

$$\tilde{s}(k_x) = \int_{-\infty}^{\infty} s(x) e^{-jk_x x} dx \tag{6.3}$$

$$\mathcal{F}^{-1}\{\tilde{s}(k_x)\} = s(x) = \frac{1}{2\pi} \int_{-\infty}^{\infty} \tilde{s}(k_x) e^{jk_x x}\, dk_x \tag{6.4}$$

or

$$\tilde{s}(k_x, k_y) = \int_{-\infty}^{\infty}\int_{-\infty}^{\infty} s(x,y) e^{-j(k_x x + k_y y)} dx dy \tag{6.5}$$

$$\mathcal{F}^{-1}\{\tilde{s}(k_x, k_y)\} = s(x,y) = \frac{1}{(2\pi)^2} \int_{-\infty}^{\infty}\int_{-\infty}^{\infty} \tilde{s}(k_x, k_y) e^{j(k_x x + k_y y)} dk_x dk_y \tag{6.6}$$

in the case of two dimensional current distributions, (6.1) can be alternatively written as

$$\overline{E}^i = \overline{\overline{\eta}} \cdot \overline{J} + \mathcal{F}^{-1}\{\tilde{\overline{\overline{\Gamma}}} \cdot \tilde{\overline{J}}\} \tag{6.7}$$

Clearly, (6.7) avoids the generation of the square matrix corresponding to the operator A implying a storage requirement of $O(N)$ as compared to $O(N^2)$ required for a moment method implementation. The solution of (6.7) via the CG method is referred to as the CGFFT solution method and the specific algorithm to be employed is given in [5] or [11].

The Fourier transforms implied in (6.7) are, of course, continuous whereas in practice they will be replaced with discrete Fourier transforms (DFTs). It is, therefore, necessary that an accurate relationship of the transforms in the discrete and continuous domains be established. Otherwise, a solution in one domain may not be representative of that in the other. Alternatively, excessive sampling may be required to represent the continuous system.

The one dimensional forward and inverse DFTs are defined as [4]

$$\hat{s}(ph) = \sum_{n=0}^{N-1} s(n\Delta) W^{np} \tag{6.8}$$

$$s(n\Delta) = s_n = \frac{1}{N} \sum_{p=0}^{N-1} [\hat{s}^\star(ph) W^{np}]^\star \tag{6.9}$$

where Δ is the integration subinterval in the spatial domain and h is the corresponding interval in the frequency domain. Also

$$W = e^{-j2\pi/N} \tag{6.10}$$

and $N = 1/\Delta h$ denotes the number of samples employed in the discretization of $s(x)$. An assumption in the derivation of the DFT pair (6.8)–(6.9) is the integral approximation

$$\int_{n\Delta - \frac{\Delta}{2}}^{n\Delta + \frac{\Delta}{2}} s(x) e^{-j2\pi hpx}\, dx \approx \Delta s_n W^{np} \tag{6.11}$$

implying that

$$s(x) e^{-j2\pi hpx} \approx s_{ro} + j s_{io} = \text{const.} \tag{6.12}$$

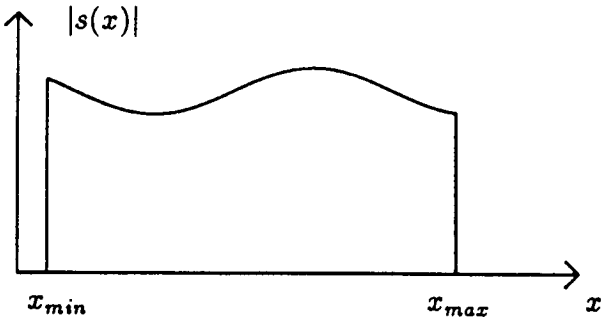

Figure 6.1 Typical spatial function $s(x)$.

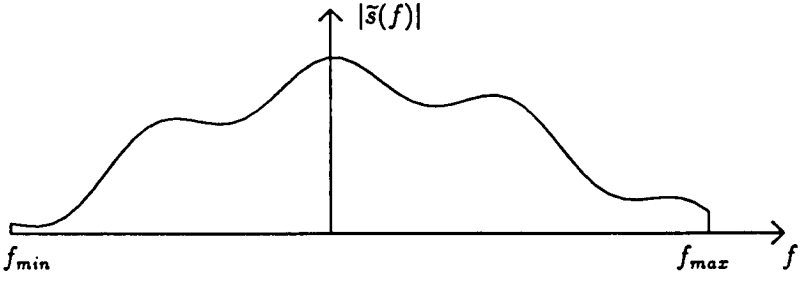

Figure 6.2 Typical spectral function $\tilde{s}(f)$.

over the subinterval. A consequence of (6.12) is that $s(x)$ is not constant over the integration subinterval [15]. In fact, it is a function of the spectral (frequency) variable and from a solution of (6.12)

$$\begin{aligned} s_r(x) &= \text{Re}\{s(x)\} = s_{ro}\cos(2\pi phx) - s_{io}\sin(2\pi phx) \\ s_i(x) &= \text{Im}\{s(x)\} = s_{ro}\sin(2\pi phx) + s_{io}\cos(2\pi phx) \end{aligned} \tag{6.13}$$

Typical forms of $s(x)$ and $\tilde{s}(k_x)$ are shown in Figs. 6.1 and 6.2, respectively. Also Fig. 6.3 illustrates the implied $s_r(x)$ at four frequencies $f = k_x/2\pi$ for the case of $s(x) = 1.0 + j\,1.0$ with $h = 1/20$ and $f_{\max} = 1/2\Delta = 10$.

It has been established [9,13] that the above inaccuracy in the implied discrete representation of a given continuous function can play

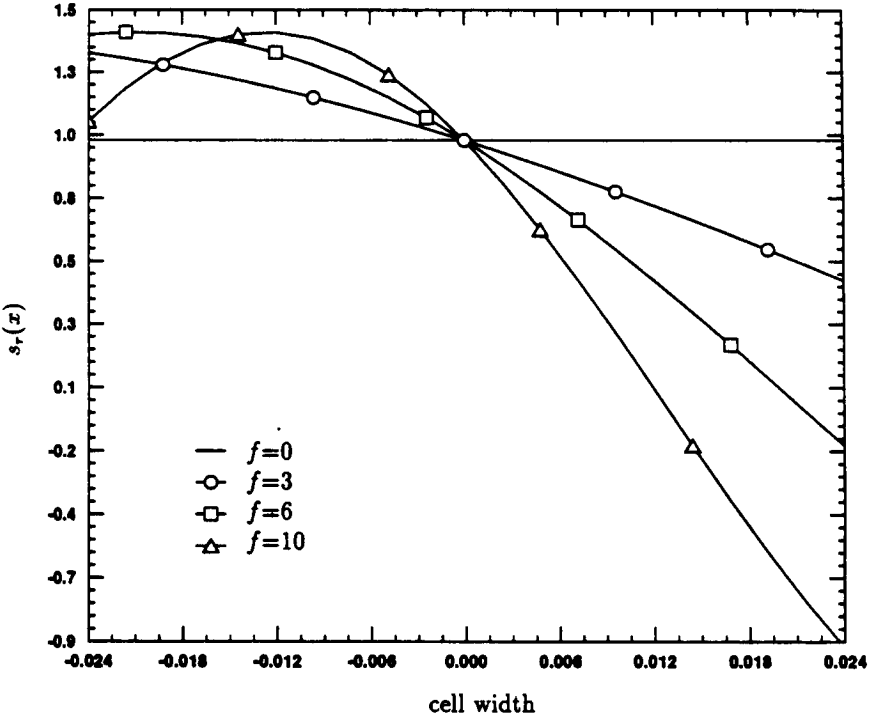

Figure 6.3 Real part of the assumed $s(x)$ at discrete frequencies.

a major role in the convergence rate of the CG solution method. It is, therefore, essential that some corrective procedure be found and an obvious approach is to employ a higher order integration formula to replace (6.11). This was discussed in [15] but as can be expected, it results in a slower DFT/FFT algorithm. An alternative [9,12,13] is to expand $s(x)$ in a sequence of subsectional basis functions $\{f_n\}$ as

$$s(x) = \sum_{n=0}^{N-1} s_n f_n(x) = \sum_{n=0}^{N-1} s_n f(x - x_n) \tag{6.14}$$

Customary forms of the basis function $f(x)$ include the piecewise constant (PWC) and the overlapping piecewise sinusoidal (PWS) expansion functions given by

$$P(x) = \begin{cases} 1, & |x| \le \Delta x/2 \\ 0, & \text{else} \end{cases} \tag{6.15}$$

$$Q(x) = \begin{cases} \frac{\sin[k_o(\Delta x - |x|)]}{\sin(k_o \Delta x)}, & |x| \leq \Delta x \\ 0, & \text{else} \end{cases} \tag{6.16}$$

respectively where $k_0 = 2\pi/\lambda_0$ denotes the wavenumber. Rewriting (6.14), $s(x)$ can now be written as a convolution in the form

$$s(x) = f(x) * \sum_{n=0}^{N-1} s_n \, \delta(x - x_n) \tag{6.17}$$

in which $\delta(x)$ is the usual Dirac delta function.

The Fourier transform of $s(x)$ is thus given by

$$\tilde{s}(k_x) = \tilde{f}(k_x) \, \hat{s} \tag{6.18}$$

where $\tilde{f}(k_x)$ is the Fourier transforms of the chosen basis function and $\hat{s}$ is a shorthand notation for the Fourier transform of the sample train as given in (6.9). Clearly, (6.18) establishes the relationship between the continuous and descret Fourier transforms. For the choices in (6.15) and (6.16),

$$\tilde{P}(k_x) = \Delta x \frac{\sin(k_x \Delta x/2)}{k_x \Delta x/2} \tag{6.19}$$

$$\tilde{Q}(k_x) = \frac{2k_0[\cos(k_x \Delta x) - \cos(k_0 \Delta x)]}{\sin(k_o \Delta x)\left(k_0^2 - k_x^2\right)} \tag{6.20}$$

and we note that as $\Delta x \to 0$

$$\tilde{s}(k_x) \approx \Delta x \hat{s}$$

which apart from the multiplying constant is the transform of $s(x)$ when $f(x) = \delta(x)$ — delta basis.

In the case of a two dimensional current representation, an appropriate expansion is

$$s(x,y) = f(x,y) * \sum_{n=0}^{N-1} \sum_{m=0}^{M-1} s_{n,m} \delta(x - x_n) \delta(y - y_m) \tag{6.21}$$

where $f(x,y)$ denotes the surface basis function and $s_{n,m} = s(x_n, y_m)$. The corresponding Fourier transform is

$$\tilde{s}(k_x, k_y) = \tilde{f}(k_x, k_y) \hat{s} \tag{6.22}$$

and consistent with the previous notation, the tilde and hat again denote the two dimensional continuous and discrete Fourier transforms, respectively. The two dimensional piecewise constant and sinusoidal basis functions are given by

$$P(x,y) = P(x)P(y) = \begin{cases} 1, & |x| < \frac{\Delta x}{2},\ |y| < \frac{\Delta y}{2} \\ 0, & \text{else} \end{cases} \tag{6.23}$$

$$\begin{aligned} Q(x,y) =& Q(x)Q(y) \\ =& \begin{cases} \frac{\sin[k_o(\Delta x - |x|)]}{\sin(k_o \Delta y)} \cdot \frac{\sin[k_o(\Delta y - |y|)]}{\sin(k_o \Delta y)}, & |x| < \Delta x,\ |y| < \Delta y \\ 0, & \text{else} \end{cases} \end{aligned} \tag{6.24}$$

Their corresponding spectra are

$$\tilde{P}(k_x,k_y) = \tilde{P}(k_x)\tilde{P}(k_y) = \Delta s \frac{\sin(k_x \Delta x/2)}{k_x \Delta x/2} \frac{\sin(k_y \Delta y/2)}{k_y \Delta y/2} \tag{6.25}$$

$$\tilde{Q}(k_x,k_y) = \tilde{Q}(k_x)\tilde{Q}(k_y) = \frac{2k_0\,[\cos(k_x \Delta x) - \cos(k_0 \Delta x)]}{\sin(k_0 \Delta x)(k_0^2 - k_x^2)} \cdot \frac{2k_0\,[\cos(k_y \Delta y) - \cos(k_0 \Delta y)]}{\sin(k_0 \Delta y)(k_0^2 - k_y^2)} \tag{6.26}$$

where $\Delta s = \Delta x \Delta y$ and as $\Delta s \to 0$, (6.22) reduces to

$$\tilde{s}(k_x,k_y) \approx \Delta s \hat{s}$$

Often, it is necessary that the basis function be chosen to have a different functionality in the x and y directions. For example, when representing the currents on a thin plate a more suitable basis function is of the form

$$f(x,y) = P(x)Q(y) \tag{6.27a}$$

or

$$f(x,y) = Q(x)P(y) \tag{6.27b}$$

having the corresponding Fourier transforms

$$\tilde{f}(x,y) = \tilde{P}(k_x)\tilde{Q}(k_y) \tag{6.28a}$$

and

$$\tilde{f}(x,y) = \tilde{Q}(k_x)\tilde{P}(k_y) \tag{6.28b}$$

respectively.

Using (6.18) or (6.22), (6.7) can now be written as

$$\overline{E}^{i} = \overline{\overline{\eta}} \cdot \overline{J} + \mathcal{F}^{-1}\left\{\overline{\overline{\tilde{\Gamma}}} \cdot \hat{\tilde{J}}\tilde{f}\right\} \tag{6.29}$$

Clearly, the transform $\tilde{f}$ of the basis function needs to be computed only once and thus the computations per iteration implied by (6.7) and (6.29) are essentially the same. It should of course be noted that (6.29) is valid only on the body of the scatterer, a condition that is imposed on the numerical solution along with the sampling requirements and linearity of the corresponding discrete convolution [4]. In a discrete implementation of (6.29), the sampling intervals should be chosen so that the Nyquist criterion is satisfied in the spatial domain. Also the length/pad of the FFT must be large enough to accommodate the spectral contents of the convolved quantities. That is, the truncation of the spectrum should cause minimal errors in the iteration process and this is another source of error in the discretization of (6.7) for a solution via the CGFFT method. This will be addressed in some detail later in the chapter but, generally, the period M of the array to be transformed is chosen according to the relation

$$M = 2^{\gamma}: \qquad M > N_{\text{Nyquist}} \qquad M \geq 2N - 1 \tag{6.30a}$$

where N is the number of unknown coefficients in the discretization of the current density and γ is an integer. In practice, γ is chosen to be the smallest integer satisfying the relation

$$\gamma \geq \log_2(2N - 1) + \rho \tag{6.30b}$$

where ρ is an integer (usually unity) setting the order of the FFT's dimension/pad. The array elements beyond the physical extent of the scatterer are set to zero before (forward) and after (inverse) transformation.

6.3 Radiation by a Thin Wire Antenna

The radiation by a center-fed cylindrical wire dipole has been extensively studied with traditional numerical techniques such as the method of moments [17-19]. It is, thus, instructive to first consider an

application of the CGFFT solution method to this problem. For a z directed cylindrical dipole of length ℓ and radius $a \ll 1$ (also $k_o a \ll 1$) the applicable integral equation is

$$E_z^i(z) = \frac{jZ_o}{k_o}\left(k_o^2 + \frac{\partial^2}{\partial z^2}\right)\int_{-\frac{\ell}{2}}^{\frac{\ell}{2}} I(z')G(z-z')dz' \tag{6.31}$$

where $I(z)$ is the total current through the wire, $Z_o = 1/Y_o$ is the free space intrinsic impedance, k_o is the wave number and $G(z,z')$ is the pertinent Green's function given by

$$G(z-z') = \frac{1}{2\pi}\int_0^{2\pi} \frac{e^{-jk_oR}}{4\pi R}\,d\phi \tag{6.32}$$

in which

$$R = \sqrt{(z-z')^2 + 4a^2\sin^2\frac{\phi}{2}} \tag{6.33}$$

Comparing (6.31) with (6.1) we may identify the right hand side of (6.31) as $A[I]$ whose adjoint is given by

$$A^a[I] = -\frac{jZ_o}{k_o}\left(k_0^2 + \frac{\partial^2}{\partial z^2}\right)\int_{-\frac{\ell}{2}}^{\frac{\ell}{2}} I(z')G^\star(z-z')dz' \tag{6.34}$$

where the $\star$ denotes complex conjugation.

A form of (6.31) compatible with (6.29) is

$$E_z^i(z) = \frac{jZ_o}{k_o}\mathcal{F}^{-1}\left\{(k_o^2 - k_z^2)\tilde{G}(k_z)\tilde{f}(k_z)\hat{I}\right\} \tag{6.35}$$

where

$$\tilde{G}(k_z) = \frac{1}{2\pi}I_0(a\sqrt{k_z^2 - k_o^2})\,K_o(a\sqrt{k_z^2 - k_o^2}) \tag{6.36}$$

is the Fourier transform of the Green's function in which I_o and K_o are the zeroth order modified Bessel functions of the first and second kind, respectively. Expression (6.35) is now suitable for a solution via the

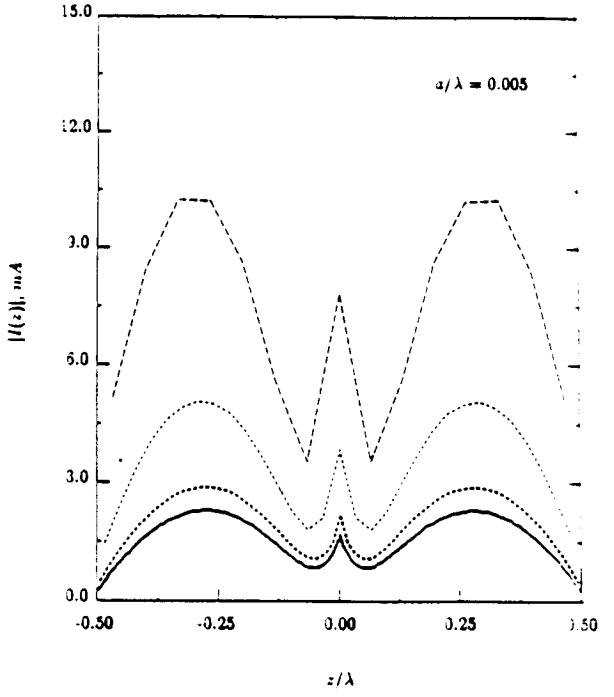

Figure 6.4(a) Numerical convergence of the linear current distribution for a $1\lambda_o$ dipole with increasing sampling density evaluated by the CGFFT. Top to bottom: No. of samples = 15,31,63,127; FFT pad order = 2,2,2,1; Magnetic frill excitation model.

CGFFT method and Figs. 6.4 – 6.6 show results based on such a solution along with comparisons based on data obtained by the method of moments (MoM) solution. In particular, Fig. 6.4 shows the convergence of the solutions as a function of sampling density using a magnetic frill model for the excitation fields and it is seen that the CGFFT and MoM solutions exhibit the same convergence characteristics. Also Fig. 6.5 depicts the convergence of the input impedance

$$Z_{in} = \frac{1}{|I(0)|^2} \int_{-\frac{\ell}{2}}^{\frac{\ell}{2}} E_z^i(z') I^*(z')\, dz' \tag{6.37}$$

as a function of sample density and it is again observed that the CGFFT and MoM[19] solutions converge to the same result. The current distribution on a $9\lambda_o$ dipole based on a voltage gap excitation

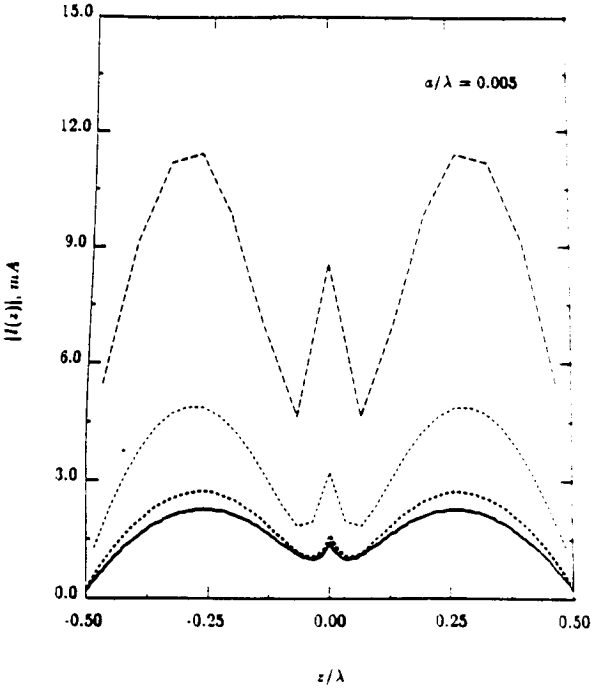

Figure 6.4(b) Numerical convergence of the linear current distribution for a $1\lambda_o$ dipole with increasing sampling density evaluated by the MoM. Top to bottom: No. of samples = 15,31,63,127; Magnetic frill excitation model.

model is given in Fig. 6.6 as predicted using a CGFFT and MoM solution. Finally, Fig. 6.7 shows the improvement in CPU time that can be achieved with the CGFFT solution method vs a MoM solution. Clearly, the CPU time required for a CGFFT solution is a linear function of the system unknowns, whereas in the case of a MoM solution the dependence is quadratic. Also, shown in Fig. 6.7 is the improved convergence attributed to the use of higher order basis functions.

6.4 Scattering by a Resistive Strip

A thin conducting sheet or dielectric layer can be represented by a resistive sheet of resistivity R ohms per unit squared. In the case of a dielectric layer having thickness τ and a relative dielectric constant

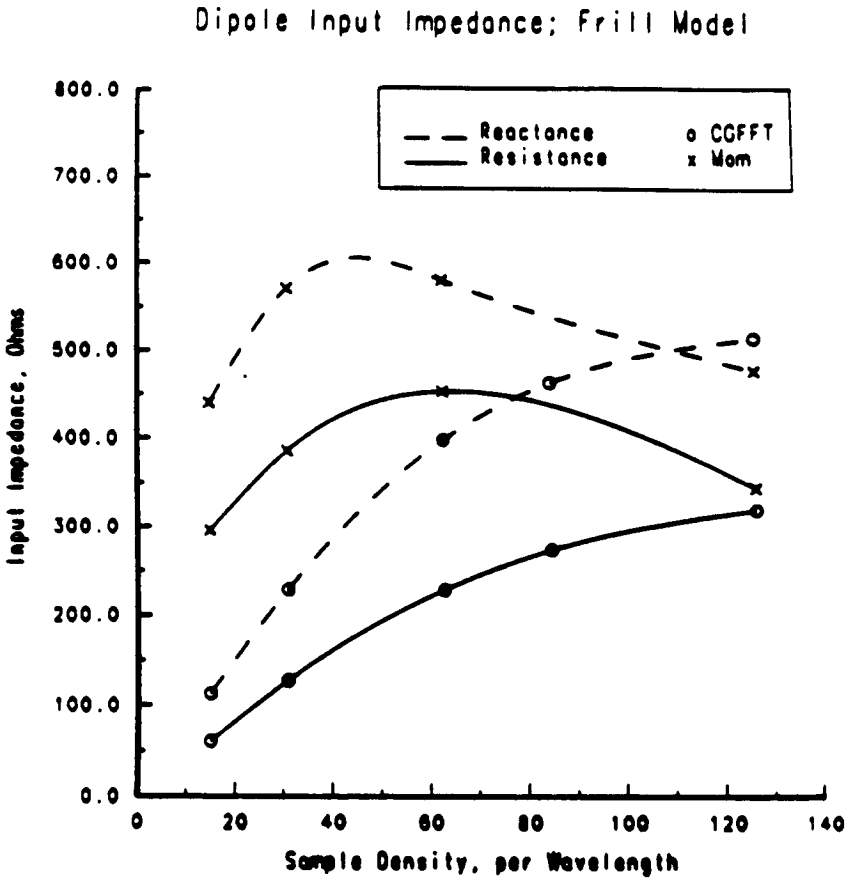

Figure 6.5 Real and imaginary parts of the input impedance for the $1\lambda_o$ dipole ($a/\lambda_o = .005$) as a function of sampling frequency.

ε_r, we find that

$$R = \frac{-jZ_0}{k_o\tau(\varepsilon_r - 1)} \tag{6.38}$$

which reduces to

$$R = \frac{Z_0}{\sigma\tau} \tag{6.39}$$

for a thin conducting sheet of conductivity σ. Mathematically, the re-

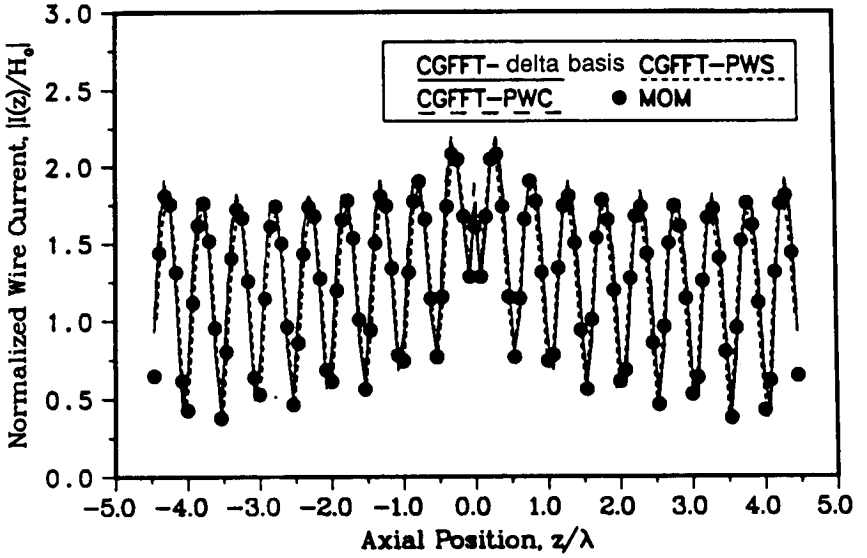

Figure 6.6 Current magnitude for a $9\lambda_o$ dipole ($a = .005\lambda_o$) computed by the MoM and the CGFFT using different basis functions and a voltage gap model for the source (13 unknown/λ_o).

sistive sheet satisfies the boundary conditions [20]

$$\begin{aligned} \hat{n} \times \hat{n} \times (\overline{E}^+ + \overline{E}^-) &= -2R\overline{J} \\ \hat{n} \times (\overline{E}^+ - \overline{E}^-) &= 0 \end{aligned} \tag{6.40}$$

in which $\overline{E}^{\pm}$ denotes the total field above and below the sheet, $\hat{n}$ is the upward unit normal to the layer and $\overline{J}$ is the supported surface current density. Using (6.40), integral equations may be derived to compute the current for a given excitation. In the following we consider their derivation and solution for E- and H-polarizations via the CGFFT method.

a. H-Polarization

Consider the H-polarized plane wave

$$\overline{H}^i = \hat{z}\, e^{jk_o(x\cos\phi_o + y\sin\phi_o)} \tag{6.41}$$

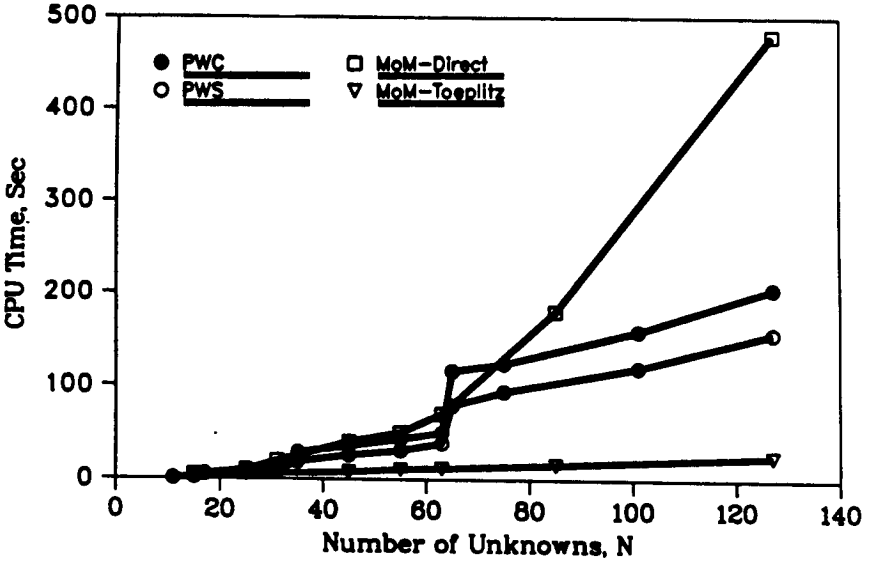

Figure 6.7 A comparison of the CPU times required by the MoM and the CGFFT for the solution of the resonant dipole problem (CGFFT tolerance: 0.003).

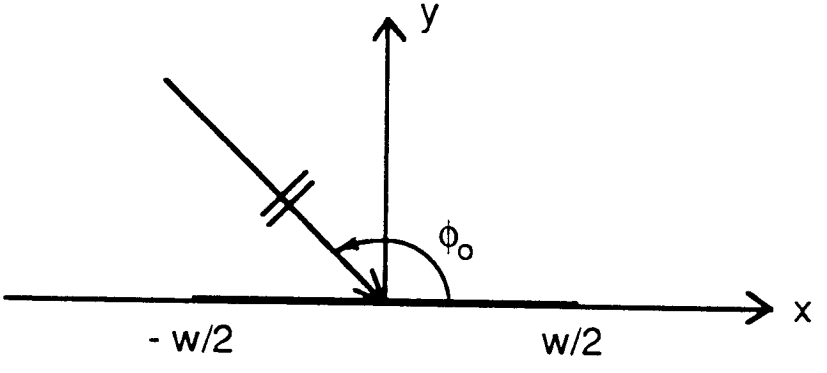

Figure 6.8 Geometry of a strip illuminated by a plane wave.

$$\overline{E}^i = Z_o(\hat{x}\sin\phi_o - \hat{y}\cos\phi_o)\, e^{jk_o(x\cos\phi_o + y\sin\phi_o)} \tag{6.42}$$

incident on the resistive strip of width w and coincident with the x-axis as shown in Fig. 6.8. This excitation generates an x-directed current, J_x, on the strip which is responsible for the scattered field. From (6.40)

the integral equation satisfied by J_x is

$$\sin\phi_o\, e^{jk_o x\cos\phi_o} = \frac{R(x)}{Z_o}J_x(x) + \frac{1}{4k_o}\left(k_0^2 + \frac{\partial^2}{\partial x^2}\right)\int_{-w/2}^{w/2} J_x(x')H_0^{(2)}(k_o|x-x'|)dx' \tag{6.43}$$

where $H_0^{(2)}(\cdot)$ is the zeroth order Hankel function of the second kind.

To solve for J_x via the CGFFT method we must rewrite (6.43) in a form compatible with (6.29). The Fourier transform of $H^{(2)}(k_o x)$ is

$$\mathcal{F}\left\{H_0^{(2)}(k_o|x|)\right\} = \tilde{H}_0^{(2)}(k_x) = \frac{2}{\sqrt{k_0^2-k_x^2}} = \frac{2j}{\sqrt{k_x^2-k_0^2}} = \frac{j}{\pi\sqrt{f_x^2-1}} \tag{6.44}$$

where $f_x = \frac{k_x}{2\pi}$, provided x is measured in wavelengths and, thus, (6.43) may be rewritten as

$$\sin\phi_o e^{jk_o x\sin\phi_o} = \frac{R(x)}{Z_o}J_x(x) + \frac{1}{4k_o}\mathcal{F}^{-1}\left\{(k_0^2-k_x^2)\tilde{H}_0^{(2)}(k_x)\hat{J}_x\tilde{f}(k_x)\right\} \tag{6.45}$$

This may now be solved via the standard CG algorithm using pulse or sinusoidal subsectional basis functions. The resulting current can then be integrated to evaluate the echowidth of the strip defined as

$$\sigma_H(\phi) = \lim_{\rho\to\infty} 2\pi\rho\left|\frac{H_z^s(\phi)}{H_z^i(\phi)}\right|^2 \tag{6.46}$$

in which (ρ,ϕ) are the usual cylindrical variables and H_z^s is the scattered field. By employing the far zone approximation for the Hankel function, we find

$$\sigma_H(\phi) = \frac{k_o}{4}\sin^2\phi\left|\int_{-w/2}^{w/2} J_x(x')e^{jk_o x'\cos\phi}dx'\right|^2 \tag{6.47}$$

In scattering computations, a usual rule in the implementation of (6.45) is to employ a sampling interval of at least 1/10 of a wavelength

and an FFT length at least twice (order 1) that of the strip in order to accommodate the spectral spreading due to the convolution, as discussed earlier. The FFT size should be chosen to minimize aliasing errors caused by the truncation of the Fourier transform of $H_0^{(2)}(k_0|x|)$. However, as seen from (6.35) and (6.45), when minimizing aliasing, the entire quantity in the curly brackets must be considered. This involves the product of the transforms of the current and Green's function and for the cases presented so far, the current densities are not expected to be associated with spatial singularities. As a result, their transform will be essentially bandlimited [1] and, thus, an FFT length of order 1 ($\rho = 1$) should be adequate to satisfy the spectral spreading due to convolution without noticeable aliasing error. However, when the current density is associated with spatial singularities as in the case of E-polarization incidence on the strip, aliasing is expected to cause substantial error unless corrective means are introduced. In general, to eliminate aliasing errors when employing the discrete Fourier transform, we must form periodic functions in the spatial and spectral domains [4] and this is the basis of the corrective procedure discussed later for E-polarization.

Echowidth patterns based on a CG solution of (6.45) are compared with MoM data in Fig. 6.9 for a strip of width $4\lambda_0$ having the given non-uniform resistivity. In practice, tapered resistive cards are often employed for radar cross section reduction and Fig. 6.10 demonstrates an example of such a reduction in connection with a strip having a resistivity that is tapered parabolically as given in Fig. 6.9. The choice of basis functions is again a factor in the convergence of the CG solution and similarly with the wire example, the sinusoidal basis functions were found to provide a substantial improvement in the convergence rate (almost 100 percent).

Before proceeding with the study of E-polarization scattering by a strip, we note that (6.43) or (6.45) are also applicable for computing the scattering by an impedance insert of width w. This simply requires the replacement of $R(x)$ by $\eta(x)/2$, where $\eta(x)$ is the (un-normalized) impedance of the insert. The resulting echowidth is then twice that given in (6.47) to account for the ground plane.

---

[1] In spite of the finite duration of the current density, we are led to this conclusion on the assumption that the processed quantity by the discrete FFT is a periodic function having period equal to twice the strip width if an order 1 FFT length is used.

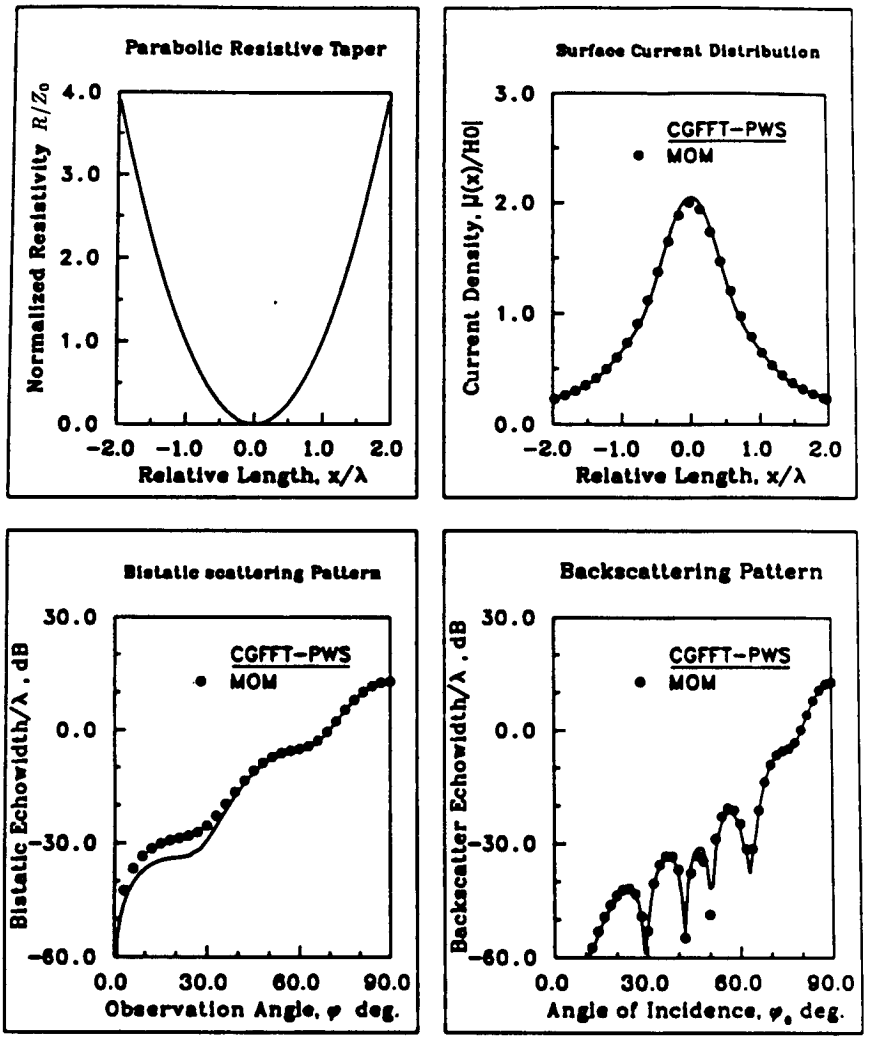

Figure 6.9 H-polarization scattering results for a $4\lambda_o$ parabolically tapered strip.

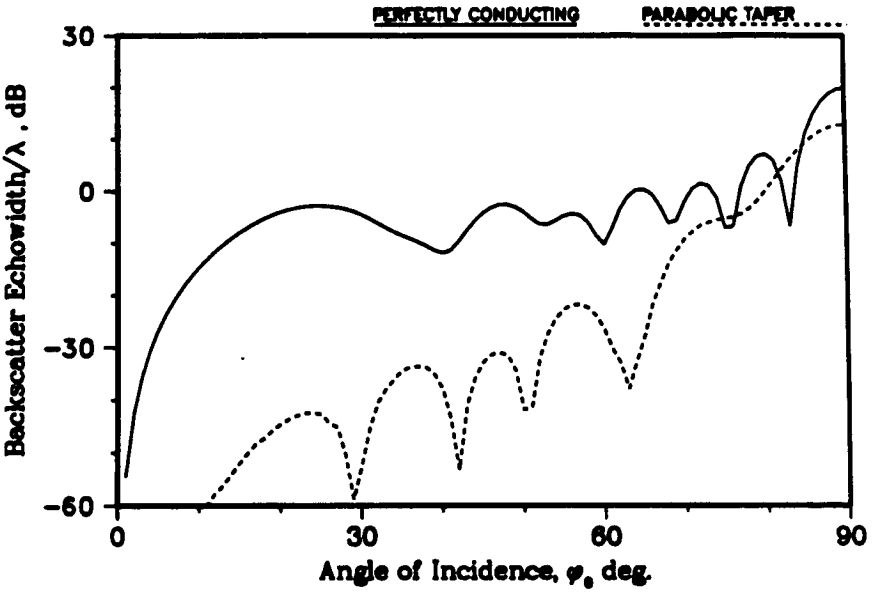

Figure 6.10 Comparison of the H-polarization backscatter echowidths of a $4\lambda_o$ perfectly conducting and parabolically tapered strips.

b. E-Polarization

Consider now the E-Polarized wave

$$\begin{aligned} \overline{E}^i &= \hat{z} e^{jk_o(x\cos\phi_o + y\sin\phi_o)} \\ \overline{H}^i &= -Z_o(\hat{x}\sin\phi_o - \hat{y}\sin\phi_o) e^{jk_o(x\cos\phi_o + y\sin\phi_o)} \end{aligned} \tag{6.48}$$

incident on the resistive strip of resistivity $R(x)$ and width w. From (6.40), this excitation generates a z-directed current density satisfying the integral equation

$$e^{jk_o x\cos\phi_o} = \frac{R(x)}{Z_o} J_z(x) + \frac{k_o}{4} \int_{-w/2}^{w/2} J_z(x') H_0^{(2)}\left(k_0|x - x'|\right)\, dx' \tag{6.49}$$

which can be rewritten as

$$e^{jk_o x \cos\phi_o} = \frac{R(x)}{Z_o} J_z(x) + \frac{k_o}{4} \mathcal{F}^{-1} \left\{ \tilde{H}_0^{(2)}(k_x) \hat{J}_z \tilde{f}(k_x) \right\} \tag{6.50}$$

for a solution via the CG method. Upon a solution of $J_z(x)$, the echowidth is now found by

$$\sigma_E(\phi) = \lim_{\rho \to \infty} 2\pi\rho \left| \frac{E_z^s(\phi)}{E_z^i(\phi)} \right|^2 = \frac{k_0}{4} \left| \int_{-w/2}^{w/2} J_z(x') e^{jkx' \cos\phi} ds' \right|^2 \tag{6.51}$$

where E_z^s is the scattered field.

The expected current behavior is now singular near the strip edges as $R(x) \to 0$ and, therefore, the unavoidable truncation of $\tilde{H}_0^{(2)}(k_x)$ will cause aliasing errors unless excessively high sampling rates are employed in the spatial and spectral domains. This is, of course, undesirable because it will increase the memory demand and execution time per iteration. However, since the integral in (6.49) calls for a knowledge of $H_0^{(2)}(k_o|x|)$ only over $-w < x < w$, we may assume it periodic with a period of $2w$ and compute its transform numerically using the discrete Fourier transform. Based on the definition of the discrete Fourier transform, aliasing is now eliminated provided the FFT length is twice the width of the strip ($2N - 1$ points, where N is the number of sample points) and the Nyquist criterion when sampling $J_z(x)$ is satisfied. Nevertheless, because of the singularity of $H_0^{(2)}(k_o|x|)$ at $x = 0$, even this approach may prove impractical and to overcome the difficulty, an alternative is to discretize the integral in (6.49) before proceeding with its computation via the discrete Fourier transform. That is, assuming a pulse basis expansion for the current density, we may write it as

$$\begin{aligned} &\int_{-w/2}^{w/2} J_z(x') H_0^{(2)}\left(k_o|x_m - x'|\right) dx' \\ &\quad = \sum_{n=0}^{N-1} J_z(x_n) \int_{x_n - \frac{\Delta_x}{2}}^{x_n + \frac{\Delta_x}{2}} H_0^{(2)}\left(k_o|x_m - x'|\right) dx' \\ &\quad = \sum_{n=0}^{N_1} J_z(x_n) g_1(x_m - x_n) \end{aligned} \tag{6.52}$$

where $x_n = -\frac{w}{2} + (n + \frac{1}{2})\Delta x$ with a similar definition for x_m and

$$g_1(x_m - x_n) \approx \begin{cases} \Delta x \left[1 - \frac{j2}{\pi}\left(\ln\frac{k_o \Delta x}{4} - 0.4228\right)\right] & n = m \\ \Delta x H_0^{(2)}(k_o|x_m - x_n|) & n \neq m \end{cases} \tag{6.53}$$

Since $g_1(x_m - x_n)$ is not singular anywhere, the evaluation of the convolution integral may now be carried out without aliasing errors via the discrete Fourier transform as

$$\int_{-w/2}^{w/2} J_z(x') H_0^{(2)}(k_o|x_m - x'|)dx' = \mathcal{F}^{-1}\left\{\hat{J}\hat{g}_1\right\} \tag{6.54}$$

where, as usual, $\hat{g}_1$ implies the discrete transform of the sample train $g_1(x_n)$. A comparison of $\tilde{H}_0^{(2)}(k_x)$ and $\hat{g}_1$ is shown in Fig. 6.11 and as expected, $\hat{g}_1$ has a ripple which is attributed to the finite duration of $g_1(x_n)$.

Expression (6.54) renders the evaluation of the integral in (6.49) relatively insensitive to the length of the FFT provided the convolution requirement is satisfied. As illustrated in Fig. 6.12 for the case of normal incidence on a perfectly conducting strip one wavelength wide, the predicted current distribution agrees with the MoM result when (6.54) is employed in the CGFFT algorithm with an FFT size just twice the length of the strip. In contrast, when employing the sampled continuous analytic transform for the evaluation of the same integral, the resulting current distribution remains in disagreement with the MoM solution even when an FFT size of order 3 is employed. The corresponding comparison of the scattering patterns is shown in Fig. 6.13 and the same observations again apply.

In closing this section, we note that the above procedure for the evaluation of a continuous convolution integral using the discrete Fourier transform can be applied at all times regardless of the expected form of the current density. To do so in conjunction with (6.45), it again amounts to replacing the sampled continuous transform $\tilde{H}_0^{(2)}(k_x)$ with $\hat{g}_1$. However, the correction will not be as evident for H-polarization. Further, for consistency, the continuous transform of the derivative

$$\mathcal{F}\left\{\frac{\partial s}{\partial x}\right\} = jk_x\tilde{s}(k_x) \tag{6.55}$$

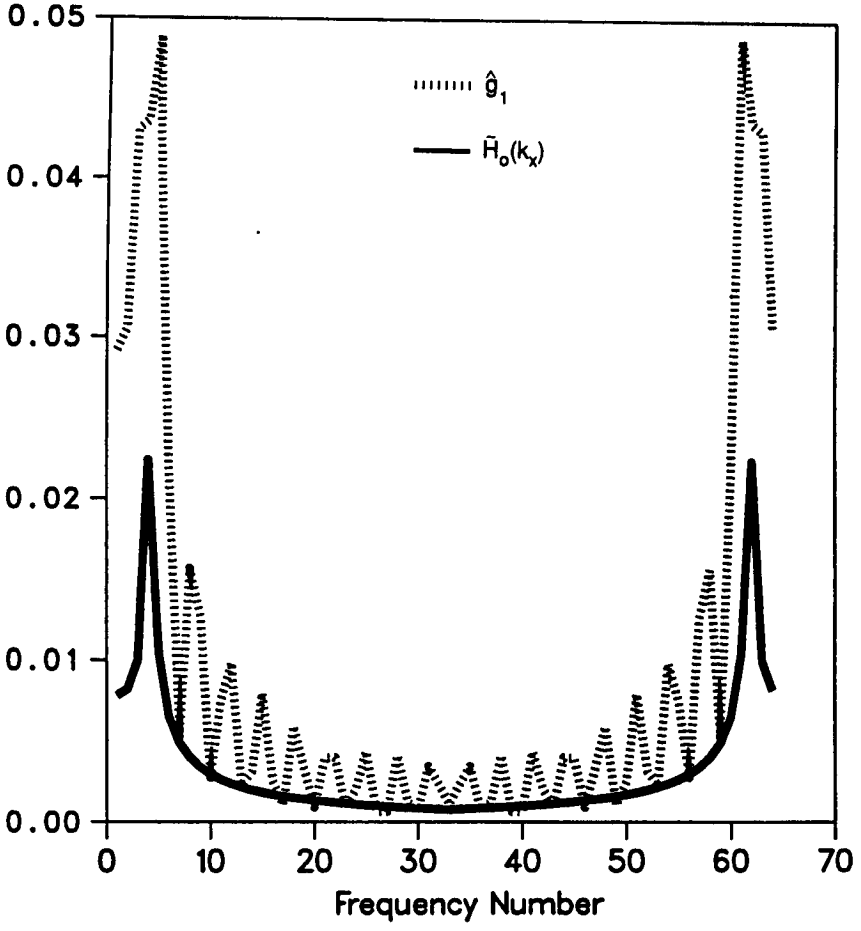

Figure 6.11 Comparison of the continuous transform of $H_o^{(2)}(k_o|x|)$ and the discrete transform of the sample train given by (6.53).

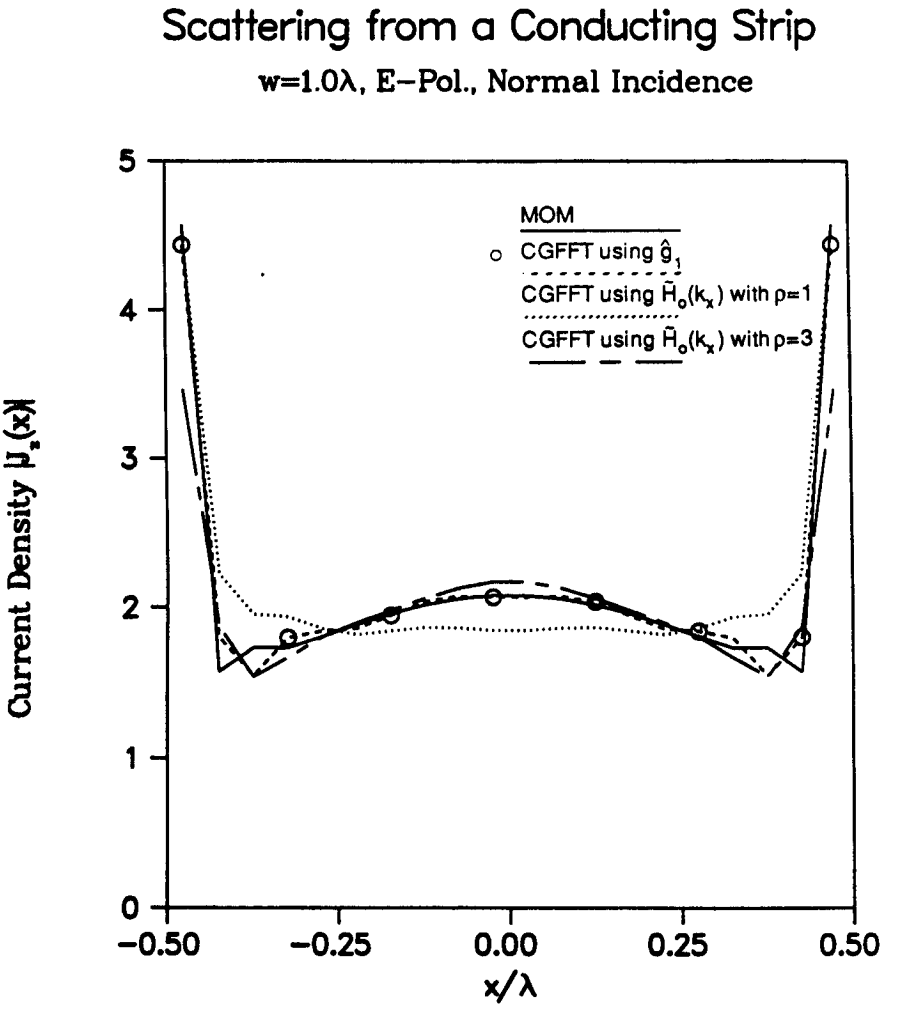

Figure 6.12 Comparison of the current distribution on a perfectly conducting strip with plane wave incidence (E-pol, $\phi_o = 0$) as computed by various methods.

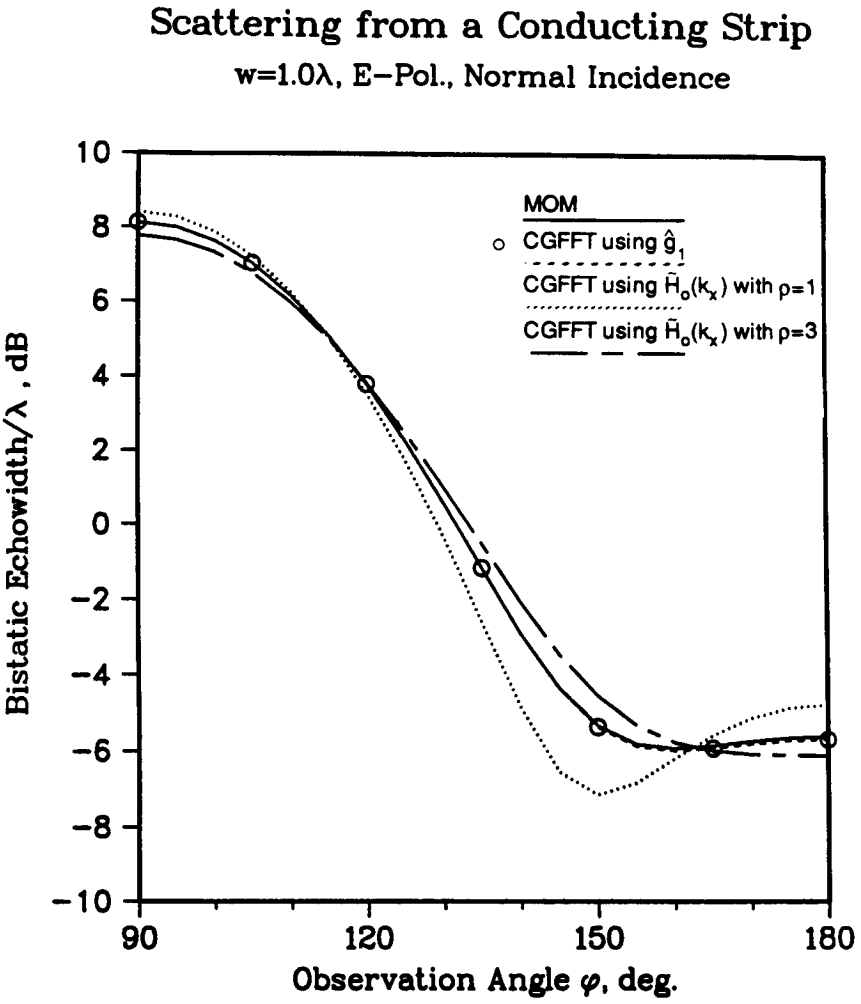

Figure 6.13 Comparison by the bistatic echowidth with plane wave incidence (E-pol, $\phi_o = 0$) as computed by various methods.

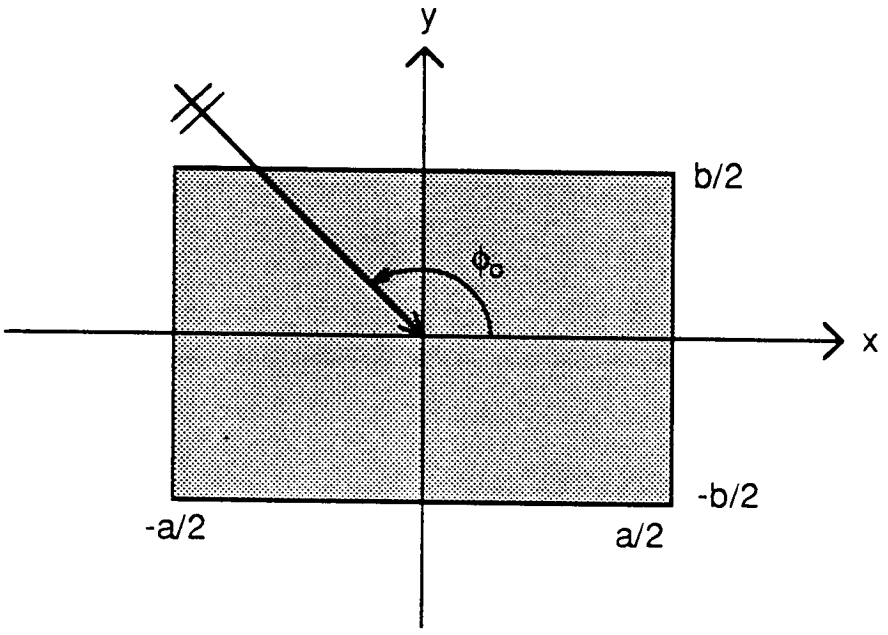

Figure 6.14 Geometry for a dielectric cylinder illuminated by a plane wave.

may also be replaced by

$$\mathcal{F}\left\{\frac{\Delta s(x)}{\Delta x}\right\} = \mathcal{F}\left\{\frac{s(x+\frac{\Delta x}{2}) - s(x-\frac{\Delta x}{2})}{\Delta x}\right\} = j\frac{2\sin(k_x\frac{\Delta x}{2})}{\Delta x}\tilde{s}(k_x) \tag{6.56}$$

as suggested in [13]. The transforms of the continuous and discrete derivatives become equal for $\Delta x \to 0$ and it is seen that the effect of the second is to suppress the high frequency components.

6.5 Scattering by a Dielectric Cylinder

Consider the dielectric cylinder shown in Fig. 6.14. We are interested in computing the scattered field due to a given excitation field $\overline{E}^i$. From [21], the scattered field due to any such excitation can be represented by the radiation of equivalent electric ($\overline{J}$) and magnetic ($\overline{M}$) currents within the volume V of the scatterer. The traditional

expressions for these are

$$\overline{J}(x,y) = \frac{jk_o}{Z_o}(\varepsilon_r - 1)\left(\overline{E}^i + \overline{E}^s\right) \qquad -\frac{a}{2} < x < \frac{a}{2}, -\frac{b}{2} < y < \frac{b}{2} \tag{6.57}$$

$$\overline{M}(x,y) = jk_o Z_o(\mu_r - 1)\left(\overline{H}^i + \overline{H}^s\right) \qquad -\frac{a}{2} < x < \frac{a}{2}, -\frac{b}{2} < y < \frac{b}{2} \tag{6.58}$$

where (ε_r, μ_r) denote the relative constitutive parameters of the dielectric cylinder and $(\overline{E}^s, \overline{H}^s)$ are the scattered fields evaluated at (x,y) within the dielectric cylinder. They represent the radiated field by the equivalent currents and can be expressed as

$$\overline{E}^s = -\frac{jZ_o}{k_o}\left(k_0^2\overline{A} + \nabla\nabla\cdot\overline{A}\right) - \nabla\times\overline{F} \tag{6.59}$$

$$\overline{H}^s = -\frac{jY_o}{k_o}\left(k_0^2\overline{F} + \nabla\nabla\cdot\overline{F}\right) + \nabla\times\overline{A} \tag{6.60}$$

with

$$\overline{A} = \iint_s \overline{J}(x',y')G(\overline{\rho},\overline{\rho}')dx'dy' \tag{6.61}$$

$$\overline{F} = \iint_s \overline{M}(x',y')G(\overline{\rho},\overline{\rho}')dx'dy' \tag{6.62}$$

being the vector potentials in which

$$G(\overline{\rho},\overline{\rho}') = -\frac{j}{4}H_0^{(2)}\left(k_o|\overline{\rho} - \overline{\rho}'|\right) \tag{6.63}$$

is the two-dimensional free space Green's function where $\overline{\rho} = x\hat{x} + y\hat{y}$ and $\overline{\rho}' = x'\hat{x} + y'\hat{y}$ are the source and observation points, respectively, and S is over the cross section of the cylinder.

Upon substitution of (6.59) and (6.60) into (6.57)–(6.58), a set of coupled integral equations are formed for the solution of $\overline{J}$ and $\overline{M}$. For non-trivial μ_r and ε_r, (6.57)–(6.58) imply three unknown current densities per volume location. In the case of H_z-incidence (see (6.41)) two tangential electric and a z-directed magnetic currents are required. Similarly, by invoking duality, in the case of E_z-incidence (see (6.48)) two tangential magnetic and a z-directed electric currents are required.

Recently [22], though, it was shown that the scattered field by an inhomogeneous dielectric cylinder can be expressed in terms of only a single current density throughout its cross-section and another current density only over the periphery of the cylinder. Unfortunately, these reduced integral equations are not amenable to a CGFFT solution. Therefore, in this section we will only consider a CGFFT solution of the traditional system implied by (6.57)–(6.60).

Let us now consider a CGFFT implementation of (6.57)–(6.60) on the assumption of H_z-incidence (see (6.41)). The corresponding solution for E_z-incidence can then be obtained via duality. Referring to the two-dimensional transform pair defined in (6.5)–(6.6) we may expand (6.59) and (6.60) to obtain

$$\begin{bmatrix} E_x^i \\ E_y^i \\ \frac{H_z^i Z_o}{k_o} \end{bmatrix} = \begin{bmatrix} Z_e J_x \\ Z_e J_y \\ \frac{\mu_r Y_m Z_o}{k_o} M_z \end{bmatrix} + \mathcal{F}^{-1}\left\{ \left[\tilde{C}_h(k_x, k_y)\right] \tilde{I}(k_x, k_y) \right\} \tag{6.64}$$

where

$$\left[\tilde{C}_h\right] = \frac{Z_o}{4k_o} \begin{bmatrix} (k_o^2 - k_x^2) & -k_x k_y & jk_y \\ -k_x k_y & (k_o^2 - k_y^2) & -jk_x \\ jk_y & -jk_x & \frac{Y_o}{k_o}(k_x^2 + k_y^2) \end{bmatrix} \tilde{H}_0^{(2)}(k_x, k_y) \tag{6.65}$$

$$\tilde{I}(k_x, k_y) = \begin{bmatrix} \hat{J}_x \\ \hat{J}_y \\ \hat{M}_z \end{bmatrix} \tilde{P}(k_x, k_y) \tag{6.66}$$

$$Z_e = \frac{-jZ_o}{(\varepsilon_r - 1)k_o}, \qquad Y_m = \frac{-jY_o}{(\mu_r - 1)k_o} \tag{6.67}$$

and $\tilde{P}(k_x, k_y)$ is the transform of the pulse basis function given in (6.25).

The two-dimensional continuous Fourier transform of the Hankel function can be obtained by noting the identity

$$\int_{-\infty}^{\infty} H_0^{(2)}\left(k_o\sqrt{x^2 + y^2}\right) e^{-jk_x x} dx = \frac{2}{\sqrt{k_0^2 - k_x^2}} e^{-j|y|\sqrt{k_0^2 - k_x^2}} \tag{6.68}$$

yielding

$$\tilde{H}_0^{(2)}(k_x, k_y) = -\frac{4j}{k_0^2 - k_x^2 - k_y^2} \tag{6.69}$$

However, as noted in the previous section, use of (6.69) in (6.65) will result in aliasing errors when truncated for implementation using the discrete FFT. An additional difficulty will also arise because of the ring singularity of (6.69) defined by $k_x^2 + k_y^2 = k_o^2$. The inherent approximation in the implementation of the inverse FFT that the transform be constant over each cell is obviously not valid for those cells coinciding with the ring singularity. This can lead to substantial errors and often the failure of the sampled or discrete system to be an acceptable representation of the continuous one.

To correct for both of the above sources of error, the procedure described earlier in connection with the one-dimensional FFT can be employed here as well. That is, the original continuous integrals are first discretized before proceeding with their evaluation via the discrete Fourier transform. This amounts to replacing $\tilde{P}(k_x, k_y)\tilde{H}_0^{(2)}(k_x, k_y)$ in (6.65) by $\hat{g}_2$ which corresponds to the discrete Fourier transform of the sample train

$$g_2(x_n, y_m) = \int_{x_n - \frac{\Delta x}{2}}^{x_n + \frac{\Delta x}{2}} \int_{y_m - \frac{\Delta y}{2}}^{y_m + \frac{\Delta y}{2}} H_0^{(2)}\left(k_o\sqrt{x'^2 + y'^2}\right) dy'dx'$$

$$\approx \begin{cases} \frac{2}{k_o^2}\left[\pi k_o \rho_o H_1^{(2)}(k_o\rho_o) - 2j\right] & x_n = y_m = 0 \\ \Delta x \Delta y H_0^{(2)}(k_o \rho_{nm}) & \text{otherwise} \end{cases} \tag{6.70}$$

in which

$$\rho_o = \sqrt{\Delta x \Delta y/\pi}, \qquad \rho_{nm} = \sqrt{x_n^2 + y_m^2} \tag{6.71}$$

and $H_1^{(2)}(\cdot)$ denotes the first order Hankel function of the second kind. For consistency, when discretizing the original integral equations (6.57) –(6.63), the continuous derivatives may also be replaced by their discrete counterparts. From a comparison of (6.55) with (6.56), this simply amounts to letting

$$k_x \to \frac{2\sin\left(\frac{k_x \Delta x}{2}\right)}{\Delta x}$$

and

$$k_y \to \frac{2\sin\left(\frac{k_y \Delta y}{2}\right)}{\Delta y}$$

wherever they appear in the matrix $[\tilde{C}_h]$.

6.6 The Material Plate

a. Formulation

In this section we consider the simulation of a thin material plate. This is an example of a three-dimensional geometry of practical interest because it represents a possible component of airframe structures. Its simulation, however, demands a large number of unknowns and, as a result, traditional matrix inversion techniques do not permit the analysis of large size plates. In contrast, the CGFFT solution method can be applied with the same ease and effectiveness as done earlier in the case of the wire and strip geometries, even as the plate size becomes as large as 100 square wavelengths. Below we first develop the necessary integral equations which are then transformed to a suitable form for a solution via the CGFFT method.

Consider the thin dielectric plate of thickness τ with $\tau \ll \lambda_p$, where λ_p is the wavelength within the material. The material plate (see Fig. 6.15) has a relative permittivity ε_r and a relative permeability μ_r. It is illuminated by an incident field $\overline{E}_i$ and we are interested in evaluating the scattered field due to the presence of the plate. As in the case of the dielectric cylinder, the traditional approach for computing the scattered field is to introduce equivalent volume electric ($\overline{J}$) and magnetic ($\overline{M}$) currents within the volume of the thin plate. Expressions (6.57)–(6.58) are still valid for this case with the dependence in z understood. However, for a thin plate we may assume that $\overline{J}$ and $\overline{M}$ are constant across the thickness of the plate and can, therefore, be replaced by the equivalent sheet currents

$$\overline{K}^e(x,y) = \tau \overline{J}(x,y,z) \tag{6.72}$$

$$\overline{K}^m(x,y) = \tau \overline{M}(x,y,z) \tag{6.73}$$

When these are employed in (6.57) – (6.58) we have

$$\overline{E}^i + \overline{E}^s = R\overline{K}^e \tag{6.74}$$

$$\overline{H}^i + \overline{H}^s = G\overline{K}^m \tag{6.75}$$

in which

$$G = \frac{-jY_o}{(\mu_r - 1)k_o\tau} = \frac{Y_m}{\tau} \tag{6.76}$$

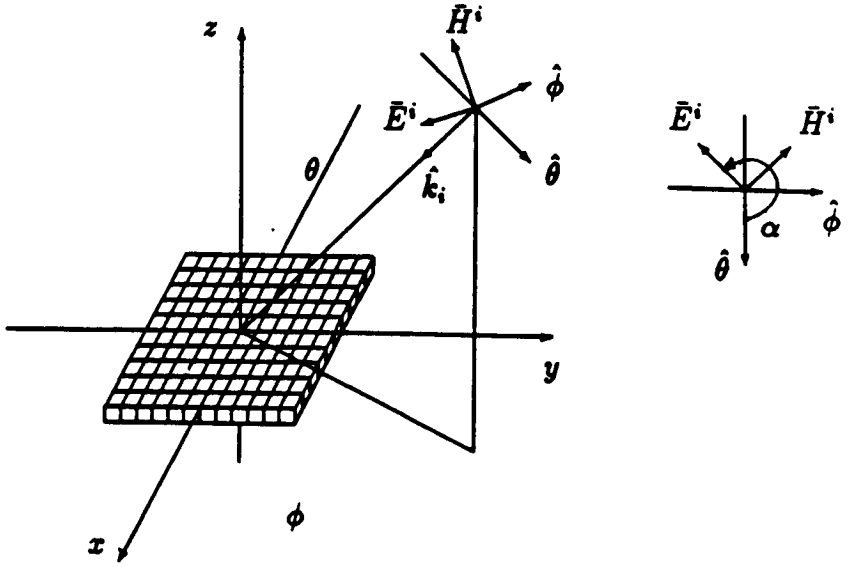

Figure 6.15 Plate geometry.

is the conductivity of the layer in mhos per square and R is the corresponding resistivity given by (6.38). The scattered fields $(\overline{E}^s, \overline{H}^s)$ are again given by (6.59) and (6.60) with the vector potentials now defined as

$$\overline{A} = \iint_S \overline{K}^e(x', y') G_o(\overline{r} - \overline{r}') dx' dy' \tag{6.77}$$

$$\overline{F} = \iint_S \overline{K}^m(x', y') G_o(\overline{r} - \overline{r}') dx' dy' \tag{6.78}$$

where S defines the surface of the plate. In these,

$$G_o(\overline{r} - \overline{r}') = \frac{e^{-jk_o|\overline{r} - \overline{r}'|}}{4\pi|\overline{r} - \overline{r}'|} \tag{6.79}$$

is the free space Green's function with

$$\bar{r} = x\hat{x} + y\hat{y} + z\hat{z}, \qquad \bar{r}' = x'\hat{x} + y'\hat{y} + z'\hat{z} \tag{6.80}$$

denoting the observation and integration points, respectively. Since the plate lies on the xy plane, $z' = 0$ and z is set to zero in the application of (6.74)–(6.75).

The integral equations satisfied by $\overline{K}^e$ and $\overline{K}^m$ are obtained from (6.74)–(6.75) once the integral expressions for the scattered fields are introduced. To write these in a concise form it is convenient to define the operators:

$$\begin{aligned}
L_1 &= k_0^2 + \tfrac{\partial^2}{\partial x^2}, & \tilde{L}_1 &= k_0^2 - k_x^2 \\
L_2 &= \tfrac{\partial^2}{\partial x \partial y}, & \tilde{L}_2 &= -k_x k_y \\
L_3 &= k_0^2 + \tfrac{\partial^2}{\partial y^2}, & \tilde{L}_3 &= k_0^2 - k_y^2 \\
L_4 &= \tfrac{\partial^2}{\partial x^2} + \tfrac{\partial^2}{\partial y^2}, & \tilde{L}_4 &= -\left(k_x^2 + k_y^2\right) \\
L_5 &= \tfrac{\partial}{\partial x}, & \tilde{L}_5 &= jk_x \\
L_6 &= \tfrac{\partial}{\partial y}, & \tilde{L}_6 &= jk_y
\end{aligned} \tag{6.81}$$

where $\mathcal{F}\{L_i\} = \tilde{L}_i$. The system satisfied by the sheet currents $\overline{K}^e = \hat{x}K_x^e + \hat{y}K_y^e + \hat{z}K_z^e$ and $\overline{K}^m = \hat{x}K_x^m + \hat{y}K_y^m + \hat{z}K_z^m$ can now be written in a matrix form as (since $\overline{K}^{e,m}$ are assumed constant across the plate thickness, all derivatives with respect to z vanish)

$$\begin{bmatrix} RK_x^e \\ RK_y^e \\ \varepsilon_r RK_z^e \\ GZ_o K_x^m \\ GZ_o K_y^m \\ \mu_r GZ_o K_z^m \end{bmatrix} + \mathcal{F}^{-1}\left\{\left[\tilde{C}(k_x,k_y)\right]\tilde{I}(k_x,k_y)\right\} = \begin{bmatrix} E_x^i \\ E_y^i \\ E_z^i \\ Z_o H_x^i \\ Z_o H_y^i \\ Z_o H_z^i \end{bmatrix} \tag{6.82}$$

in which

$$\left[\tilde{C}(k_x,k_y)\right] = \begin{bmatrix} c_o\tilde{L}_1 & c_o\tilde{L}_2 & 0 & 0 & 0 & \tilde{L}_6 \\ c_o\tilde{L}_2 & c_o\tilde{L}_3 & 0 & 0 & 0 & -\tilde{L}_5 \\ 0 & 0 & -c_o\tilde{L}_4 & -\tilde{L}_6 & \tilde{L}_5 & 0 \\ 0 & 0 & -\tilde{L}_6 & c_o\tilde{L}_1 & c_o\tilde{L}_2 & 0 \\ 0 & 0 & \tilde{L}_5 & c_o\tilde{L}_2 & c_o\tilde{L}_3 & 0 \\ \tilde{L}_6 & -\tilde{L}_5 & 0 & 0 & 0 & -c_o\tilde{L}_4 \end{bmatrix} \tilde{G}_o(k_x,k_y) \tag{6.83}$$

with $c_o = \frac{j}{k_o}$,

$$\tilde{I}(k_x, k_y) = \left[Z_o \hat{K}_x^e, Z_o \hat{K}_y^e, Z_o \hat{K}_z^e, \hat{K}_x^m, \hat{K}_y^m, \hat{K}_z^m \right]^T \tilde{P}(k_x, k_y) \quad (6.84)$$

and

$$\tilde{G}_o(k_x, k_y) = \begin{cases} \frac{1}{2j\sqrt{k_0^2 - k_x^2 - k_y^2}}, & k_x^2 + k_y^2 < k_0^2 \\ \frac{1}{2\sqrt{k_x^2 + k_y^2 - k_0^2}}, & k_x^2 + k_y^2 > k_0^2 \end{cases} \quad (6.85)$$

is the continuous Fourier transform of the free space Green's function. As usual, $\hat{K}_x^{e,m}, \hat{K}_y^{e,m}$ and $\hat{K}_z^{e,m}$ denote the discrete transforms of the corresponding sampled current densities. Also, to avoid aliasing as well as limit the required FFT pad to order 1, $\tilde{G}_o(k_x, k_y)\tilde{P}(k_x, k_y)$ should be replaced by the discrete transform of the sample train

$$\begin{aligned} g_0(x_n, y_m) &= \int_{x_n - \frac{\Delta x}{2}}^{x_n + \frac{\Delta x}{2}} \int_{y_m - \frac{\Delta y}{2}}^{y_m + \frac{\Delta y}{2}} \frac{e^{-jk_o\sqrt{x'^2 + y'^2}}}{4\pi\sqrt{x'^2 + y'^2}} dy dx \\ &\approx \begin{cases} \frac{\rho_o}{2} e^{-jk_o\rho_o/2} \frac{\sin\left(\frac{k_o\rho_o}{2}\right)}{\left(\frac{k_o\rho_o}{2}\right)} & x_n = y_m = 0 \\ \frac{e^{-jk_o\rho_{nm}}}{4\pi\rho_{nm}} \Delta x \Delta y & \text{otherwise} \end{cases} \end{aligned} \quad (6.86)$$

with ρ_o and ρ_{nm} as defined in (6.71). Further, the replacements for k_x and k_y suggested in the previous section could be introduced in (6.81) if so desired. We note that (6.86) has been shown to be of acceptable accuracy when $\Delta x = \Delta y \leq 0.1\lambda_o$.

It should be noted from an examination of the matrix in (6.83) that not all currents are coupled. Specifically, $K_{x,y}^e$ and K_z^m may be solved independently from the remaining three currents. As a result, the entire system may be split into half for a more efficient solution on a machine having a vector-concurrent facility as discussed in a later section. Finally, we observe that the matrix $[\tilde{C}(k_x, k_y)]$ is symmetric and, therefore, the adjoint of the systems (6.82) needed in the execution of the CG algorithm is easily found provided we replace K_z^m by $-K_z^m$.

Often, of interest is the simulation of resistive plates satisfying the boundary condition (6.40). In that case, only the first two equations of the system (6.82) are required with K_x^e and K_y^e being the only non zero currents. We, thus, have

$$R \begin{bmatrix} K_x^e \\ K_y^e \end{bmatrix} + c_o Z_o \mathcal{F}^{-1} \begin{Bmatrix} \left(\tilde{L}_1 \hat{K}_x^e + \tilde{L}_2 \hat{K}_y^e \right) \hat{g}_o \\ \left(\tilde{L}_2 \hat{K}_x^e + \tilde{L}_3 \hat{K}_y^e \right) \hat{g}_o \end{Bmatrix} = \begin{bmatrix} E_x^i \\ E_y^i \end{bmatrix} \quad (6.87)$$

valid for a resistive plate of resistivity R. When $R = 0$, then (6.87) represent the system for the surface currents on a perfectly conducting plate.

The systems (6.82) and (6.87) are, of course, suitable for a solution via the CG method. Upon evaluation of the currents $\overline{K}^e$ and $\overline{K}^m$ the scattered field is given as

$$\overline{E}^s(\theta,\phi) = jk_o \frac{e^{-jkr}}{4\pi r} \left[\hat{r} \times \overline{N}_t^m(\theta,\phi) - Z_o N_t^e(\theta,\phi)\right] \tag{6.88}$$

where (r,θ,ϕ) are the spherical coordinates of the observation point and

$$\hat{r} = \frac{\overline{r}}{|\overline{r}|} = \frac{\overline{r}}{r} \tag{6.89}$$

Also,

$$\overline{N}_t^{e,m}(\theta,\phi) = \hat{\theta} N_{t\theta}^{e,m}(\theta,\phi) + \hat{\phi} N_{t\phi}^{e,m}(\theta,\phi) \tag{6.90}$$

$$\begin{aligned} N_{t\theta}^{e,m}(\theta,\phi) = \cos\theta \left[\cos\phi S_x^{e,m}(\theta,\phi) + \sin\phi S_y^{e,m}(\theta,\phi)\right] \\ - \sin\theta S_z^{e,m}(\theta,\phi) \end{aligned} \tag{6.91}$$

$$N_{t\phi}^{e,m}(\theta,\phi) = -\sin\phi S_x^{e,m}(\theta,\phi) + \cos\phi S_y^{e,m}(\theta,\phi) \tag{6.92}$$

and

$$\overline{S}^{e,m}(\theta,\phi) = \iint\limits_{\text{plate}} \overline{K}^{e,m}(x',y') e^{jk_o \cos\theta [x' \cos\theta + y' \sin\theta]} dx'dy' \tag{6.93}$$

The field $\overline{E}^s$ can also be described as that attributed to the radiation of the plate currents and is responsible for the radar cross section of the plate defined as

$$\sigma = \lim_{r\to\infty} \quad 4\pi r^2 \frac{|\overline{E}^s \cdot \hat{p}_r|^2}{|\overline{E}^i|^2} \tag{6.94}$$

in which $\hat{p}_r$ is a unit vector denoting the polarization of the receiving antenna.

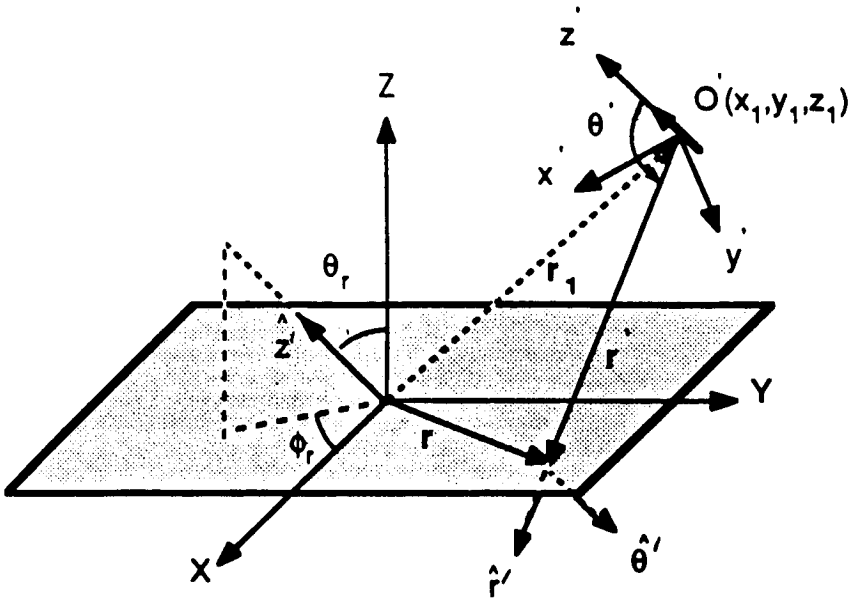

Figure 6.16 Geometry of an arbitrarily oriented Hertzian dipole in the vicinity of a plate.

b. Applications

1. Radiation of a dipole in the presence of a plate

In this subsection we consider a few applications to radiation and scattering associated with a material plate. As a first example, we consider the problem of radiation by a Hertzian dipole in the presence of a resistive plate, illustrated in Fig. 6.16. The dipole is centered at (x_1, y_1, z_1), is of length $\ell (\ell \ll \lambda_o)$ and carries a constant excitation current equal to unity. Its presence excites currents on the resistive plate which contribute to the overall radiation pattern. To compute the plate currents we must solve the system (6.87) with the incident field given as

$$E_x^i = (E_{r'}\hat{r}' + E_{\theta'}\hat{\theta}') \cdot \hat{x} \tag{6.95}$$

$$E_y^i = (E_{r'}\hat{r}' + E_{\theta'}\hat{\theta}') \cdot \hat{y} \tag{6.96}$$

where the primes indicate spherical system parameters measured with

respect to the coordinate system at the dipole as shown in Fig. 6.16. We have

$$E_{r'} = 2Z_o k_o \ell \left(1 + \frac{1}{jk_o r'}\right) \frac{e^{-jk_o r'}}{4\pi k_o r'^2} (\hat{z}' \cdot \hat{r}') \tag{6.97}$$

$$E_{\theta'} = jZ_o k_o \ell \left[1 + \frac{1}{jk_o r'} - \frac{1}{(k_o r')^2}\right] \frac{e^{-jk_o r'}}{4\pi r'} \sqrt{1 - (\hat{z}' \cdot \hat{r}')^2} \tag{6.98}$$

in which $\hat{z}'$ denotes the dipole orientation and can be represented as

$$\hat{z}' = \cos\phi_r \sin\theta_r \hat{x} + \sin\phi_r \sin\phi_r \hat{y} + \cos\theta_r \hat{z} \tag{6.99}$$

where (θ_r, ϕ_r) are the spherical angles of the dipole axis with respect to the plate's coordinate system. Also, $\overline{r}' = r'\hat{r}'$ is the vector drawn from the dipole's location to the observation point on the plate and

$$\hat{\theta}' = \frac{\hat{z}' \times \hat{r}'}{|\hat{z}' \times \hat{r}'|} \times \hat{r}' \tag{6.100}$$

Radiation patterns based on a solution of (6.87) are given in Figs. 6.17 and 6.18. In particular, Fig. 6.17 illustrates the dominant current component on a perfectly conducting and a resistive $1\lambda_o \times 1\lambda_o$ rectangular plate due to illumination by a horizontal electric dipole $\lambda_o/4$ above the center of the plate. Fig. 6.18 shows a principal plane radiation pattern due to a vertical dipole also $\lambda_o/4$ above the center of the plate. As seen, the pattern computed with the CGFFT is in good agreement with that based on the MoM technique [23].

2. Plane wave scattering by perfectly conducting and resistive plates

Plates have been of considerable interest in scattering because they often represent building blocks in the simulation of more complex configurations of practical interest. An understanding of their scattering characteristics can, therefore, provide insightful information for design applications. In this case, simple high frequency formulae are usually more suitable, but unfortunately, available expressions have not been found to yield accurate results. On the other hand, numerical simulations demand an excessive storage requirement making the CGFFT solution method attractive for such simulations.

Consider the plate in Fig. 6.15 illuminated by a plane wave of unity amplitude. If

$$\overline{k}_i = -k_o(\hat{x}\cos\phi_i \sin\theta_i + \hat{y}\sin\phi_i \sin\theta_i + \hat{z}\cos\theta_i) \tag{6.101}$$

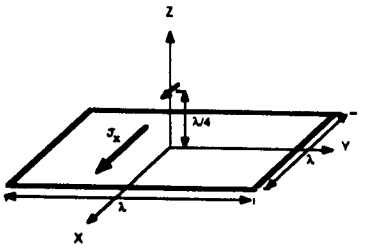

(a)

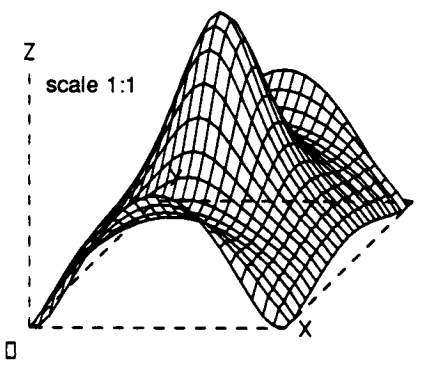

(b)

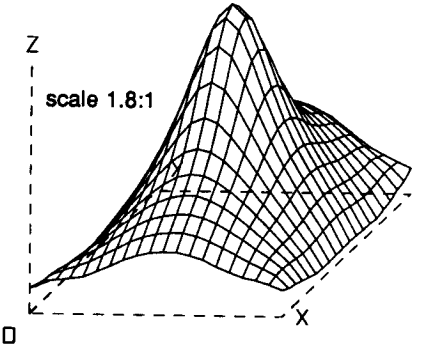

(c)

Figure 6.17 The like-polarized component of the surface current density on a $1\lambda_o \times 1\lambda_o$ plate excited by a horizontal Hertzian dipole $\lambda_o/4$ above the center of the plate (25 × 25 unknowns). (a) plate geometry, (b) current distribution on a perfectly conducting plate, (c) current distribution on a resistive plate.

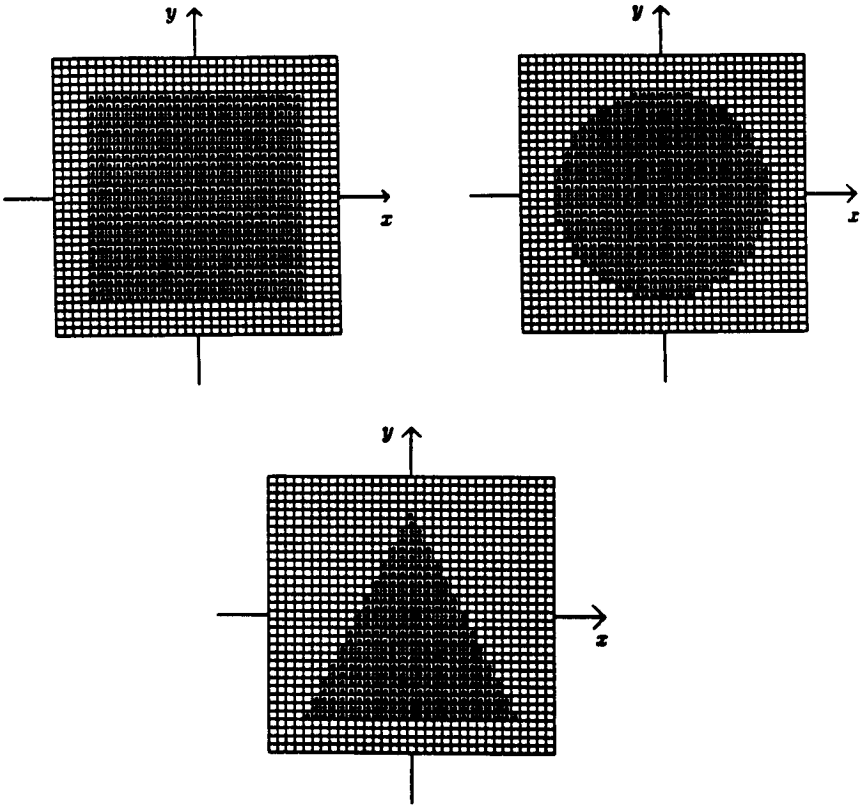

Figure 6.19 Examples of discretized plate geometries.

For a perfectly conducting or a resistive plate, the system (6.87) is applicable for the solution of the electric currents generated on the plate due to a plane wave illumination. Using a computer program based on a CGFFT algorithm, computations were performed for a variety of plate sizes and shapes. These are shown in Fig. 6.19 and as seen, their discrete model is a collection of rectangular cells. At first, it is of interest to examine the current distributions on the rectangular plate. It will be seen that these have a rather unique and predictable behavior, particularly for principal plane incidences.

Figures 6.20 – 6.25 depict three-dimensional views of the like and cross-polarization currents on rectangular plates. Specifically, Figs. 6. 20 – 6.22 [25] illustrate currents on a $2\lambda_o \times 2\lambda_o$ plate for E-polarization ($\alpha_i = 90°$) with $\theta_i = 0, \phi_i = 0$ (normal incidence); $\theta_i = 45°$, $\phi_i = 0$, and $\theta_i = 90°$, $\phi_i = 0$. Some important observations with regards to these plots are the high current density values near the edges and the increasing significance of the cross polarization currents as θ increases. For example, at normal incidence the like-polarized currents are more than five times larger than the cross-polarized (K_x^e) currents indicating that K_x^e is not significant and this is consistent with the physical optics approximation. The singular behavior of the K_y^e currents at the edges is, of course, noteworthy and generic to perfectly conducting structures with sharp edges. These singularities are responsible for the diffracted fields and are the primary source of difficulty in numerical simulations. As θ increases, the strength of the cross-polarization currents also increases effecting the behavior of the like-polarized currents, especially those toward the back edge of the plate. When $\theta = 90°$, K_x^e have their greatest strength. They are concentrated near the side edges and are responsible for the travelling edge waves which, although not radiating at backscatter, are crucial in determining the back edge like-polarized current behavior. The lobing structure of the edge currents is particularly interesting and unique to all rectangular plates regardless of their size. For example, a similar current behavior is observed in the case of a $5\lambda_o \times 5\lambda_o$ and a $10\lambda_o \times 10\lambda_o$ plate as illustrated in Figs. 6.23 and 6.24, respectively. Generally, we may conclude that for a $n\lambda_o \times n\lambda_o$ plate, the magnitude of the like-polarized currents are associated with n maxima near the front and back edges, whereas the cross polarized currents have $2n$ maxima near the side edges. Unfortunately, this current behavior is not maintained for non-principal plane incidences, as demonstrated in Fig. 6.25, although the singular edge behavior of the

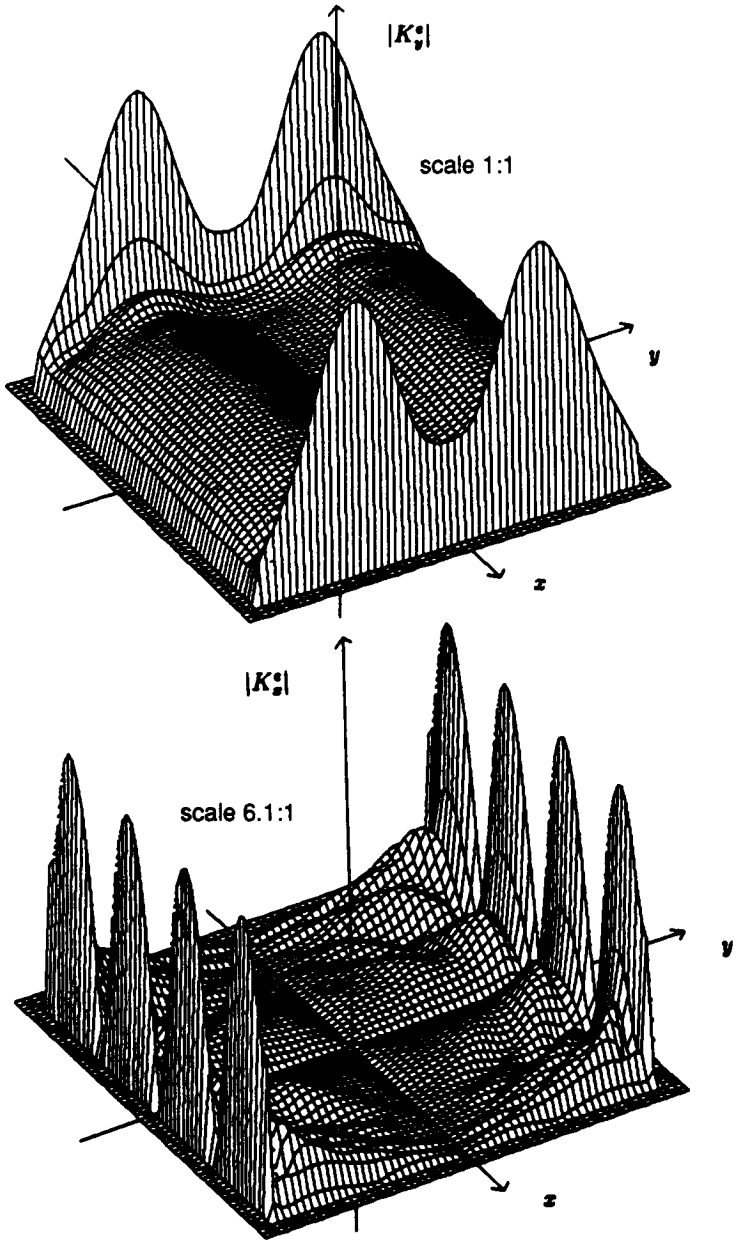

Figure 6.20 Conducting plate currents; Polarization: $\alpha_i = 90°$, Direction of incidence: $\phi_i = 0, \theta_i = 0$, Plate size: $2\lambda_o \times 2\lambda_o$, No. of samples: 55×55, No. of iterations: 100, Normal residual: 0.00919.

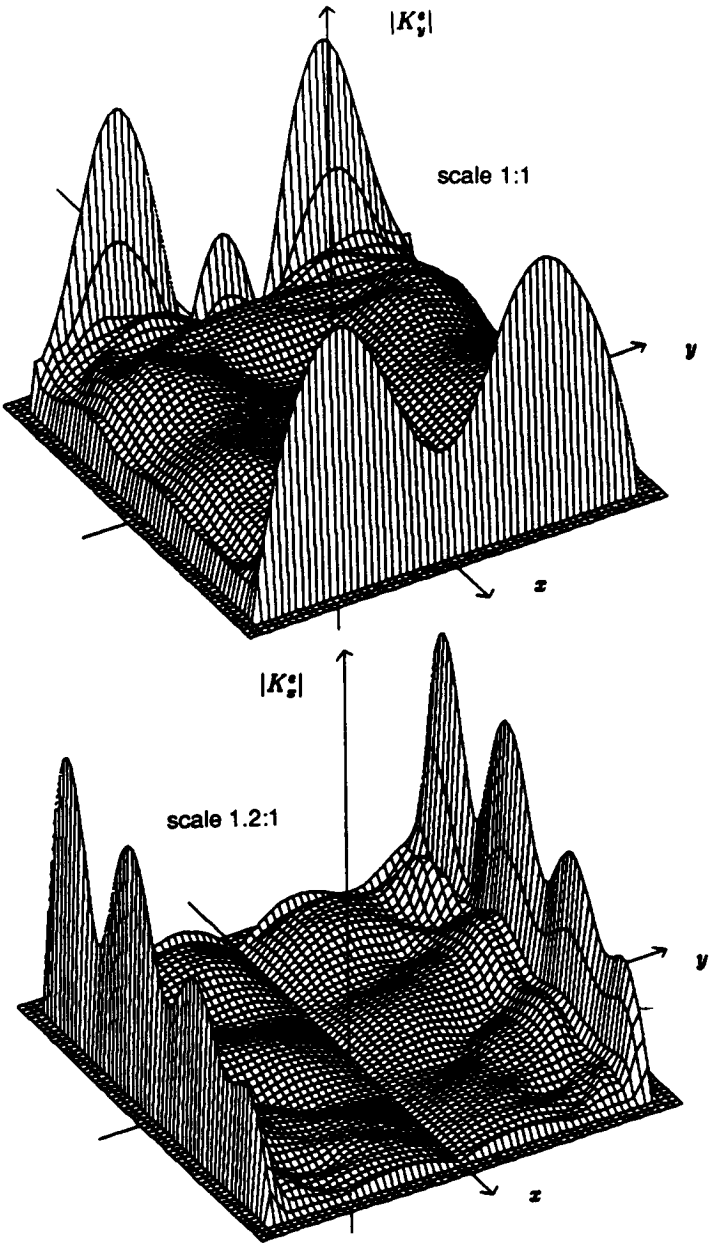

Figure 6.21 Conducting plate currents; Polarization: $\alpha_i = 90°$, Direction of incidence: $\phi_i = 0, \theta_i = 45°$; Plate size: $2\lambda_o \times 2\lambda_o$; No. of samples: 55×55; FFT pad size: 120×120; No. of iterations: 100; Normal residual: 0.01489.

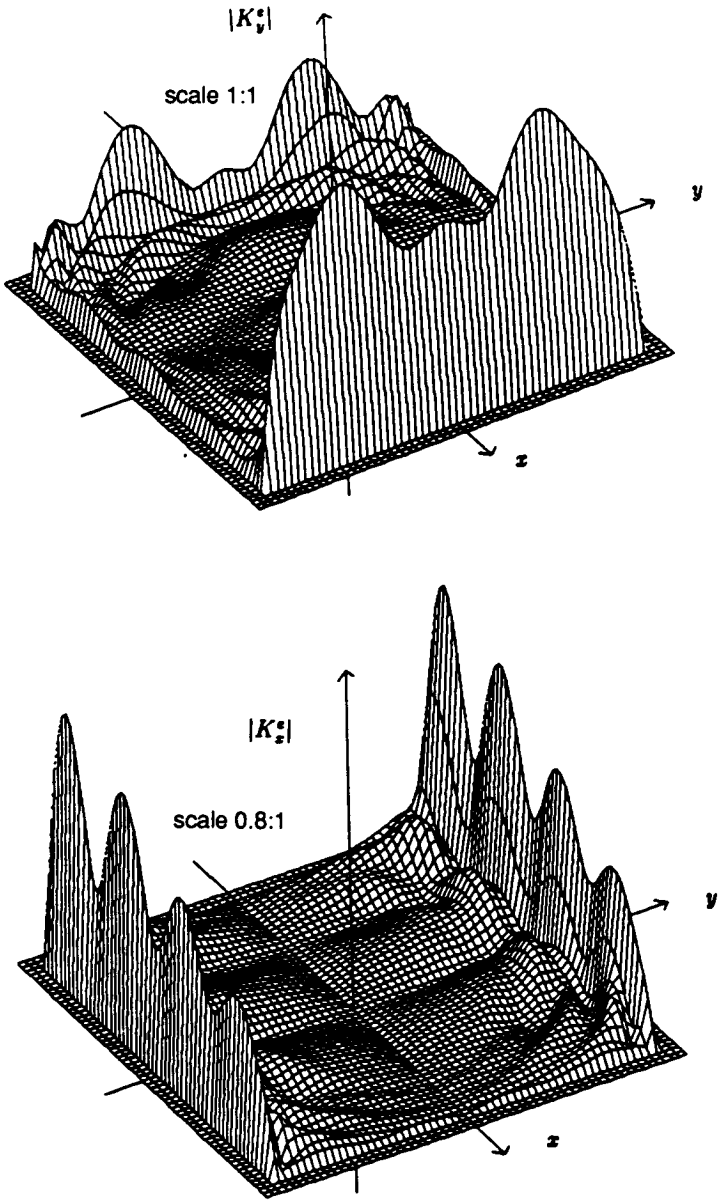

Figure 6.22 Conducting plate currents; Polarization: $\alpha_i = 90°$, Direction of incidence: $\phi_i = 0$, $\theta_i = 90°$, Plate size: $2\lambda_o \times 2\lambda_o$; No. of samples: 55×55; No. of iterations: 100; Norm. Residual: 0.02942.

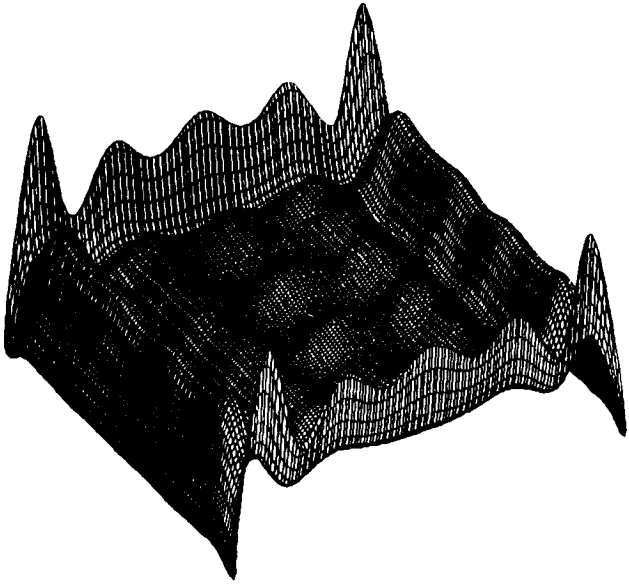

Figure 6.23 Like polarized conducting plate currents; Polarization: $\alpha_i = 90°$, Direction of incidence: $\phi_i = 0$, $\theta_i = 0°$, Plate size: $5\lambda_o \times 5\lambda_o$; No. of samples: 125×125; FFT pad size: 256×256.

current densities is still apparent.

As expected, (see Fig. 6.26) the current densities associated with a resistive or dielectric (possibly with moderate loss tangent) plate do not exhibit such singularities near the edges and are also associated with small cross polarized currents. This translates to faster convergence in the CGFFT solution and also implies that a physical optics calculation is suitable for far zone scattering computations [24].

Using the computed plate current densities the radar cross section (RCS) of the plate can be found in accordance with (6.88)–(6.94). Since the RCS of a structure is an easily measured quantity, it provides a means for validating the CGFFT solution. Figs. 6.27 to 6.29 show principal plane backscatter RCS patterns as computed via the CGFFT

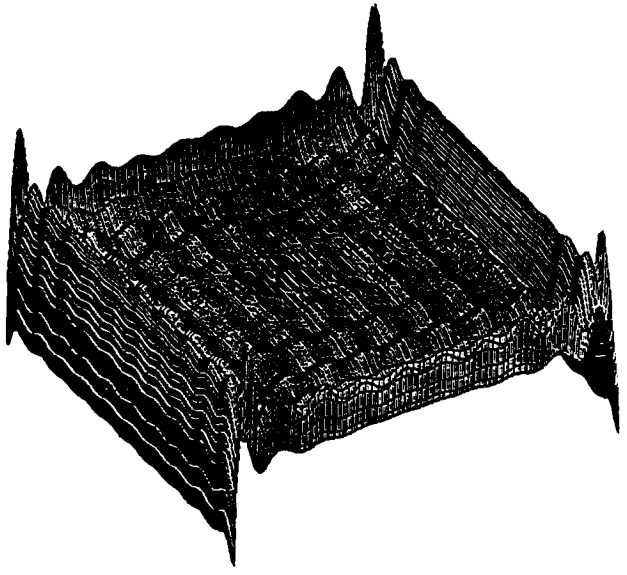

Figure 6.24 Like polarized conducting plate currents; Polarization: $\alpha_i = 90°$, Direction of incidence: $\phi_i = 0$, $\theta_i = 0°$, Plate size: $10\lambda_o \times 10\lambda_o$; No. of samples: 250×250; FFT pad size: 512×512.

for square, triangular and circular plates. Both, E- and H-polarization patterns are given and, as shown, in all cases the agreement with measured data is very good. It should be noted that the calculation of the currents associated with the conducting plate in Fig. 6.24 required nearly 125,000 unknowns. This large number of unknowns presents a challenge for direct matrix inversion approaches because of their large storage requirement. In contrast, the CGFFT solution could be performed on a relatively small computer.

The computation of volumetric backscatter RCS patterns requires an excessive computation time since the CGFFT solution must be repeated for each incidence angle. Some time savings can indeed be realized by employing the solution of a previous incidence as the starting

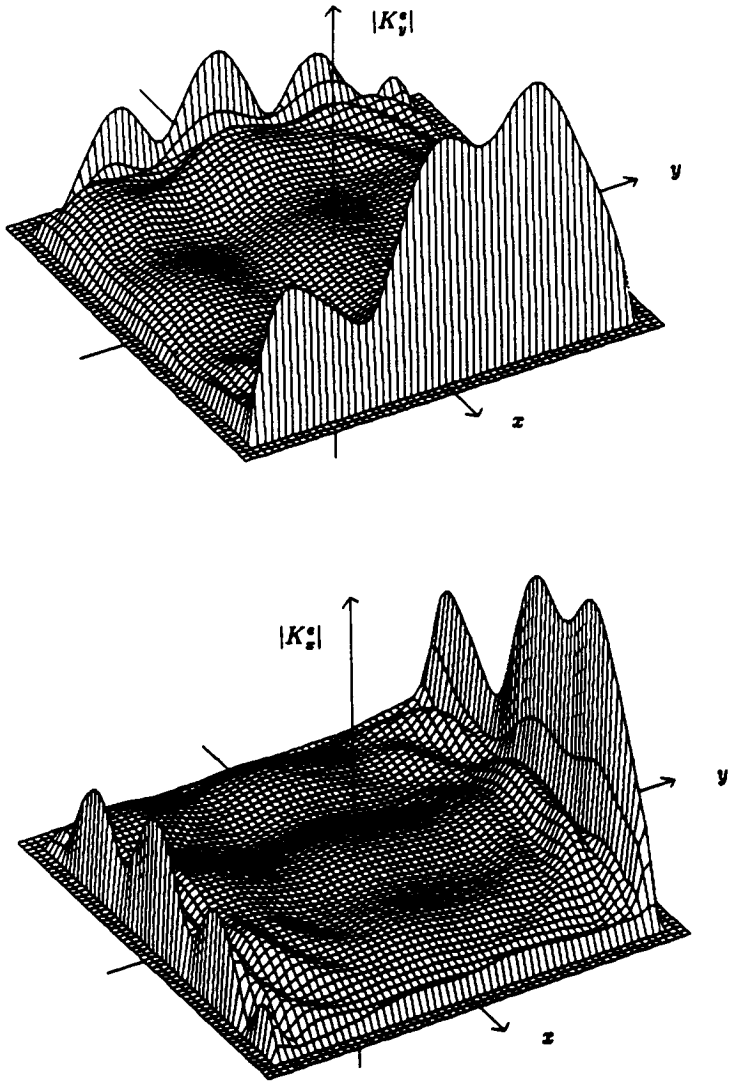

Figure 6.25 Conducting plate currents; Polarization: $\alpha_i = 90°$, **Direction of incidence:** $\phi_i = 45$, $\theta_i = 45°$, **Plate size:** $2\lambda_o \times 2\lambda_o$; **No. of samples:** 55×55; **No. of iterations:** 100; **Normal residual:** 0.01275.

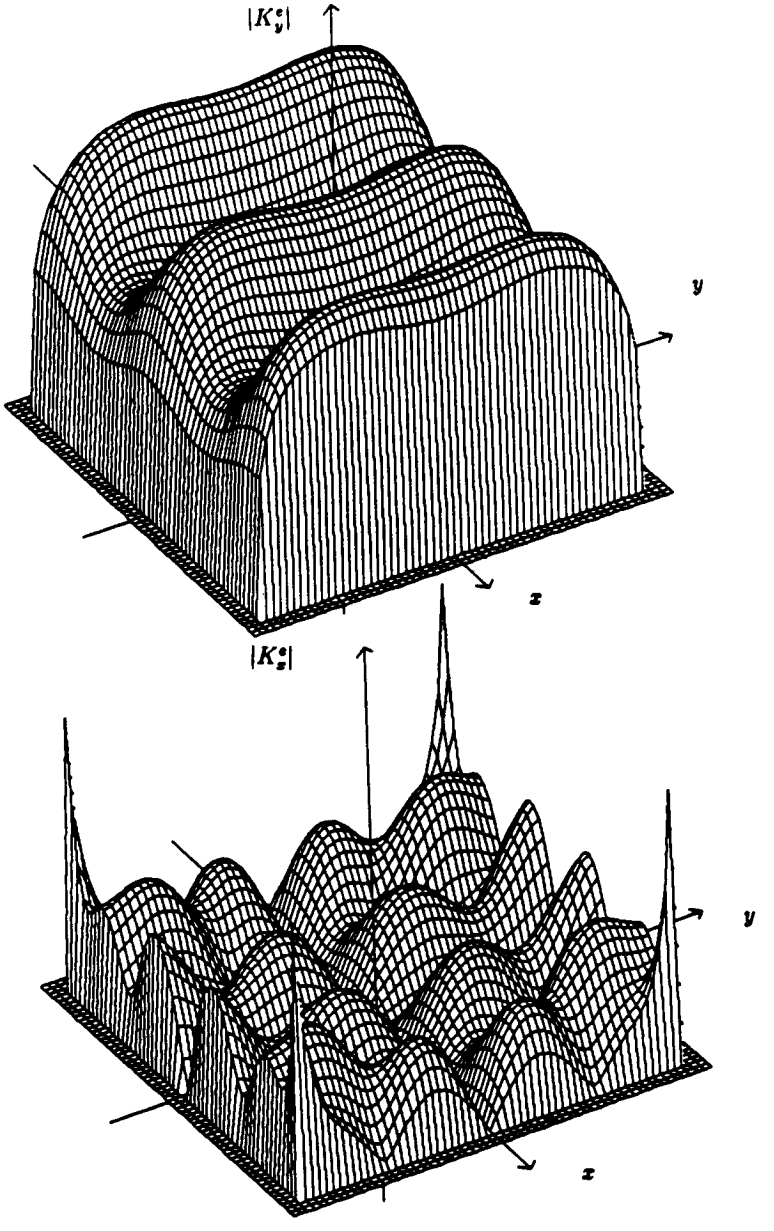

Figure 6.26 Dielectric plate currents; Polarization: $\alpha_i = 90°$, Direction of incidence: $\phi_i = 0, \theta_i = 0°$, Plate size: $2\lambda_o \times 2\lambda_o$; Plate thickness: 0.0254λ; Plate constitutive parameters: $\varepsilon_r = 7.4 - j1.11, \mu_r = 1$; No. of samples: 55×55; No. of iterations: 52; Normal residual: 0.00001.

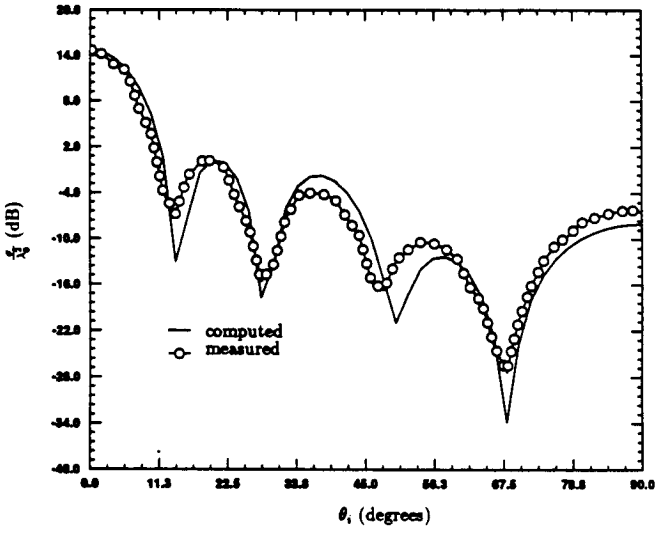

(a)

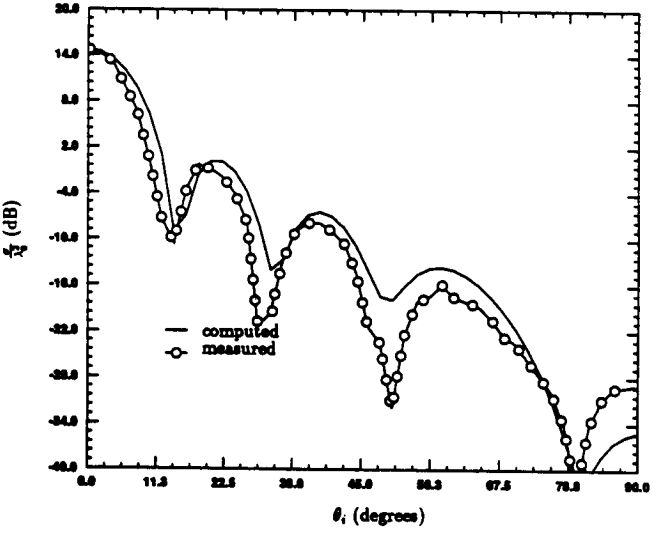

(b)

Figure 6.27 Backscatter patterns from a square material plate; Plate size: $2\lambda_o \times 2\lambda_o$; Plate thickness: $\tau = 0.0254\lambda_o$; Plate relative constitutive parameters: $\varepsilon_r = 7.4 - j1.11, \mu_r = 1.4 - j0.672$; No. of samples: 39×39; Max. No. of iterations: 50 per angle. (a) $\alpha_i = 90°$, $\phi_i = 0°$, average normalized residual error = 0.0014, (b) $\alpha_i = 0°$, $\phi_i = 0°$, average normalized residual error = 0.003.

point for the next, but even then the overall computation time for a volumetric pattern remains substantial. However, volumetric bistatic patterns can be easily computed and Fig. 6.30 shows one such pattern for a perfectly conducting $2\lambda_o \times 2\lambda_o$ plate [25].

6.7 Coated Perfectly Conducting Plate

The material coated plate consists of a perfectly conducting plate having one face covered with a thin material layer of the same dimensions. Mathematically, it may be simulated by a pair of stacked layers and in this manner we may construct any arbitrary three dimensional structure. A study of the scattering by the coated plate, therefore, represents a step toward the simulation of general three dimensional configurations.

Consider the plane wave (6.102)–(6.104) illuminating the coated plate configuration shown in Fig. 6.31. To compute the scattered field due to this excitation we introduce the usual equivalent electric ($\overline{J}_2$) and a magnetic ($\overline{M}_2$) currents within the dielectric. Also an electric current sheet

$$\overline{K}_1^e = \hat{x}K_{x1}^e + \hat{y}K_{y1}^e \tag{6.107}$$

must be introduced on the perfectly conducting plate located at $z = 0$. Further, on the assumption of a thin coating/layer, $\overline{J}_2$ and $\overline{M}_2$ may be replaced by the sheet currents

$$\begin{aligned} \overline{K}_2^e &= \tau\overline{J}_2 = \hat{x}K_{x2}^e + \hat{y}K_{y2}^e + \hat{z}K_{z2}^e \\ \overline{K}_2^m &= \tau\overline{M}_2 = \hat{x}K_{x2}^m + \hat{y}_{y2}^m + \hat{z}K_{z2}^m \end{aligned} \tag{6.108}$$

placed at $z = \tau/2$, the center of the coating.

For a coating having relative constitutive parameters (ε_r, μ_r), the boundary conditions satisfied by the sheet currents are (see (6.57)–(6.58))

$$\begin{aligned} \overline{E}^i + \overline{E}^s &= R\overline{K}_2^e \quad ; \quad z = \tau/2 \\ \overline{H}^i + \overline{H}^s &= G\overline{K}_2^m \quad ; \quad z = \tau/2 \\ \overline{E}^i + \overline{E}^s &= 0 \quad ; \quad z = 0 \end{aligned} \tag{6.109}$$

with R and G as defined in (6.38) and (6.76). The vector potentials employed in the definition of the scattered fields (6.59)–(6.60) are now

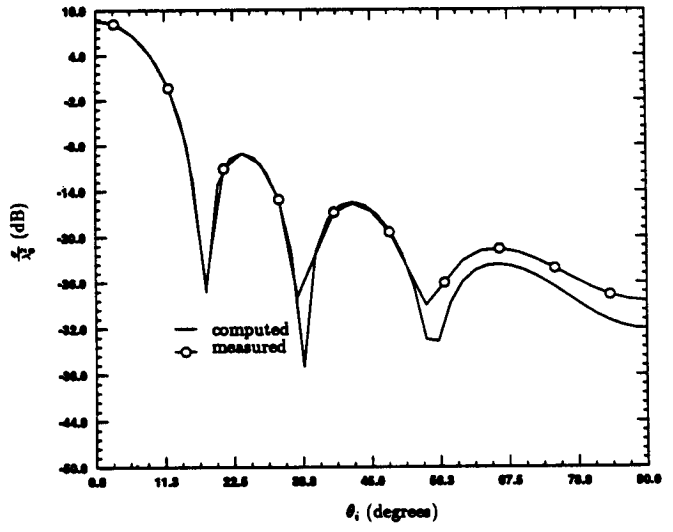

(a)

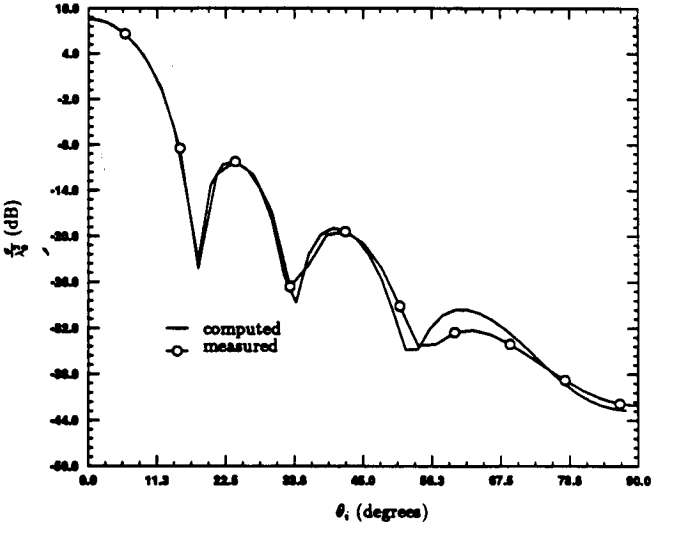

(b)

Figure 6.28 Backscatter patterns from a circular dielectric plate; Plate radius: λ_o; Plate thickness $= 0.01\lambda_o$; Plate relative constitutive parameters: $\varepsilon_r = 2 - j10, \mu_r = 1$; No. of samples: 39×39; Max. No. of iterations: 50 per angle. (a) $\alpha_i = 90°, \phi_i = 0°$, average normalized residual error $=$ 0.00006, (b) $\alpha_i = 0°, \phi_i = 0°$, average normalized residual error $= 0.00007$.

given by

$$\begin{aligned}\overline{A} &= \int\int_{\text{plate}} \overline{K}_1^e(x',y')G_o(\overline{r}-\overline{r}_1')dx'dy' \\ &+ \int\int_{\text{plate}} \overline{K}_2^e(x',y')G_o(\overline{r}-\overline{r}_2')dx'dy' \\ \overline{F} &= \int\int_{\text{plate}} \overline{K}_2^m(x',y')G_o(\overline{r}-\overline{r}_2')dx'dy'\end{aligned} \tag{6.110}$$

where

$$\overline{r}_1' = x'\hat{x}+y'\hat{y}, \qquad \overline{r}_2' = x'\hat{x}+y'\hat{y}+\tau/2\hat{z} \tag{6.111}$$

$G_o(\overline{r},\overline{r}')$ has been defined in (6.79) and $\overline{r}$ is the observation vector given in (6.80). For convenience, let us also define the vectors

$$\overline{r}_1 = x\hat{x}+y\hat{y}, \qquad \overline{r}_2 = x\hat{x}+y\hat{y}+\tau/2\hat{z} \tag{6.112}$$

and employ the notation

$$\begin{aligned}\overline{A}^{ij} &= \int\int_{\text{plate}} \overline{K}_j^e(x',y')G_o(\overline{r}_i-\overline{r}_j')dx'dy' \\ \overline{F}^{ij} &= \int\int_{\text{plate}} \overline{K}_j^m(x',y')G_o(\overline{r}_i-\overline{r}_j')dx'dy'\end{aligned} \tag{6.113}$$

From (6.109), the integral equations satisfied by the currents can now be expressed as [25]

$$\begin{aligned}c_0Z_0L_1\left[A_x^{11}+A_x^{12}\right] &+ c_0Z_0L_2\left[A_y^{11}+A_y^{12}\right] \\ &+ c_0Z_0L_5\frac{\partial}{\partial z}A_x^{12} - \frac{\partial}{\partial z}F_y^{12} + L_6F_x^{12} = E_{x1}^i \\ c_0Z_0L_2\left[A_x^{11}+A_x^{12}\right] &+ c_0Z_0L_3\left[A_y^{11}+A_y^{12}\right] \\ &+ c_0Z_0L_6\frac{\partial}{\partial z}A_z^{12} + \frac{\partial}{\partial z}F_x^{12} - L_5F_x^{12} = E_{y1}^i \\ RK_{x2}^e &+ c_0Z_0L_1\left[A_x^{21}+A_x^{22}\right] \\ &+ c_0Z_0L_2\left[A_y^{21}+A_y^{22}\right] + L_6F_z^{22} = E_{x2}^i \\ RK_{y2}^e &+ c_0Z_0L_2\left[A_x^{21}+A_x^{22}\right]\end{aligned}$$

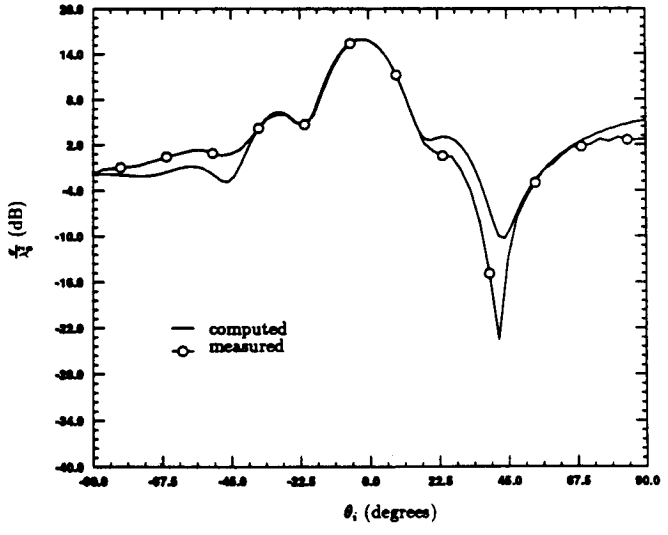

(a)

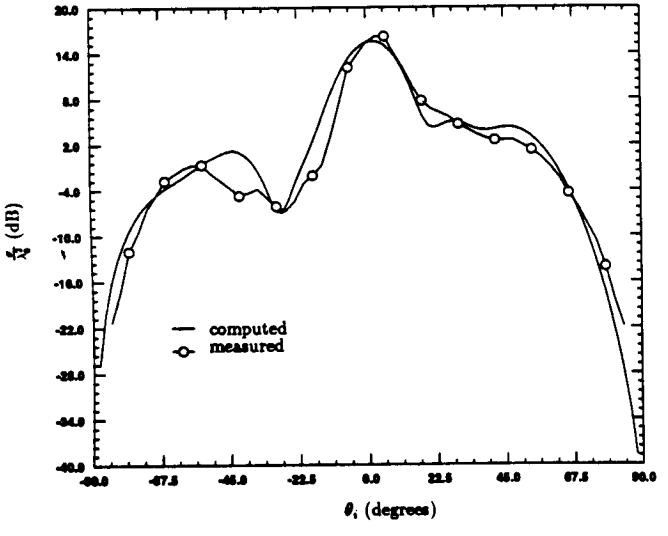

(b)

Figure 6.29 Backscatter patterns from a perfectly conducting equilateral triangular plate ($\theta_i = 90°$ corresponds to tip-on); Plate side length = $2\lambda_o$; No. of samples: 39 × 39; Max. No. of iterations: 50 per angle. (a) $\alpha_i = 90°, \phi_i = 0°$, average normalized residual error = 0.032, (b) $\alpha_i = 0°, \phi_i = 0°$, average normalized residual error = 0.079.

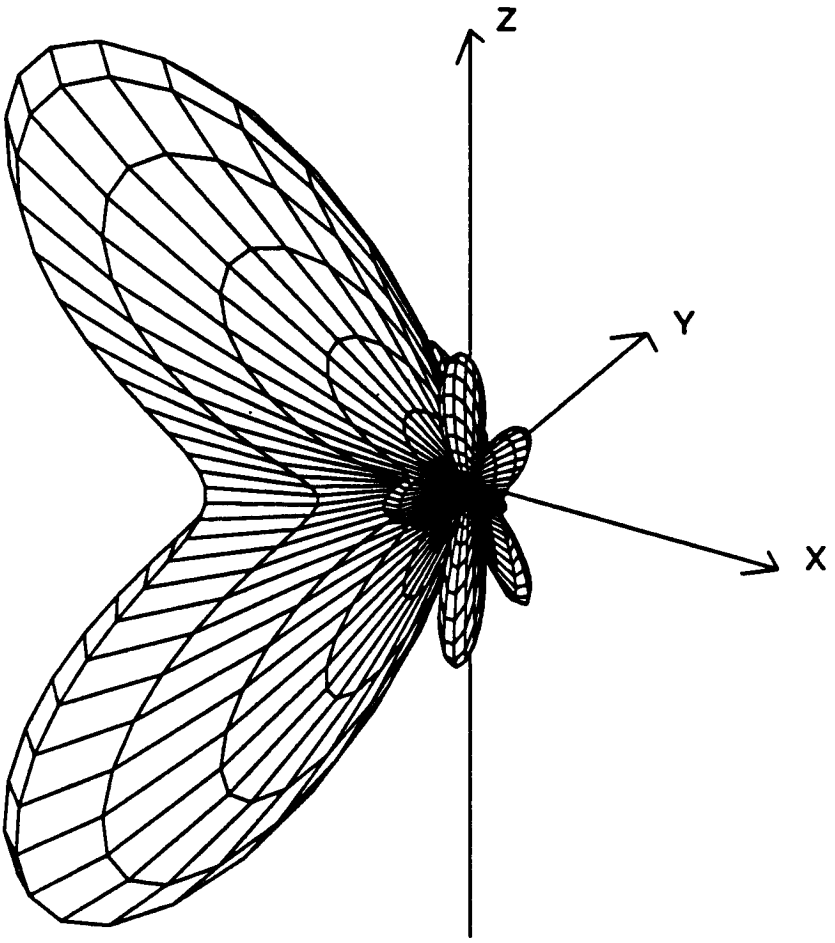

Figure 6.30 Bistatic pattern for a perfectly conducting square plate; Plate size $= 2\lambda_o \times 2\lambda_o$; No. of samples: 35×35; $\phi_i = 30°, \theta_i = 45°$.

$$+ c_0 Z_0 L_3 \left[A_y^{21} + A_y^{22}\right] - L_5 F_x^{22} = E_{z2}^i$$

$$\varepsilon_r R K_{z2}^e + c_0 Z_0 L_5 \frac{\partial}{\partial z} A_x^{21} + c_0 Z_0 L_6 \frac{\partial}{\partial z} A_y^{21}$$
$$- c_0 Z_0 L_4 A_z^{22} - L_6 F_x^{22} + L_5 F_y^{22} = E_{z2}^i$$

$$G Z_0 K_{x2}^m + Z_o \frac{\partial}{\partial z} A_y^{21} + c_0 L_1 F_x^{22}$$

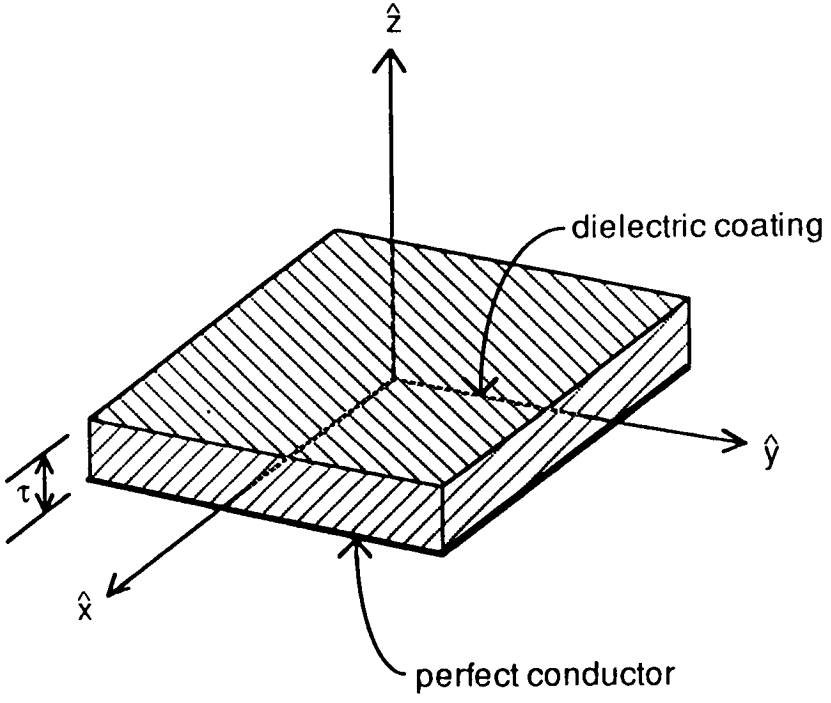

Figure 6.31 Geometry of a dielectrically coated perfectly conducting plate.

$$+ c_0 L_2 F_y^{22} - Z_0 L_6 A_z^{22} = Z_0 H_{x2}^i$$

$$\begin{aligned} GZ_0 K_{y2}^m - Z_o \frac{\partial}{\partial z} A_x^{21} + c_0 L_2 F_x^{22} \\ + c_0 L_3 F_y^{22} + Z_0 L_5 A_z^{22} = Z_0 H_{y2}^i \\ \mu_r G Z_0 K_{z2}^m + Z_0 L_6 \left[A_x^{21} + A_x^{22}\right] - Z_0 L_5 \\ \left[A_y^{21} + A_y^{22}\right] - c_0 L_4 F_z^{22} = Z_o H_{z2}^i \end{aligned} \quad (6.114)$$

where L_i are the operators defined in (6.81), $c_o = j/k_o$ and we have assumed a constant field variation across the thickness of the coating. Also, $\overline{E}_1^i$ denotes the electric field observed at $z = 0$ and likewise $(\overline{E}_2^i, \overline{H}_2^i)$ denotes the fields measured at $z = \tau/2$.

The entire system (6.114) involves a total of eight unknown sheet currents to represent the presence of the coated plate. On the assumption of a non-magnetic coating ($\mu_r = 1$), $\overline{K}_2^m$ vanishes and thus only the first five equations of the system (6.114) are required for the simulation of the coated plate. Further, in the case of E-polarization ($E_z^i = 0$)$K_{z2}^e = 0$ and the system (6.114) reduces to

$$\begin{aligned}
c_0 L_1 \left[A_x^{11} + A_x^{12}\right] + c_0 L_2 \left[A_y^{11} + A_y^{12}\right] &= E_{x1}^i \\
c_0 L_2 \left[A_x^{11} + A_x^{12}\right] + c_0 L_3 \left[A_y^{11} + A_y^{12}\right] &= E_{y1}^i \\
RK_{x2}^e + c_0 L_1 \left[A_x^{21} + A_x^{22}\right] + c_0 L_2 \left[A_y^{21} + A_y^{22}\right] &= E_{x2}^i \\
RK_{y2}^e + c_0 L_2 \left[A_x^{21} + A_x^{22}\right] + c_0 L_3 \left[A_y^{21} + A_y^{22}\right] &= E_{y2}^i
\end{aligned} \tag{6.115}$$

To write (6.114) or (6.115) in a form compatible with (6.29) for a CGFFT solution we note the relations

$$L_m \overline{A}^{ii} = \mathcal{F}^{-1}\left\{\tilde{L}_m \hat{\overline{K}}_i^e \tilde{P}(k_x, k_y)\tilde{G}_o(k_x, k_y)\right\} \tag{6.116}$$

$$L_m \overline{A}^{ij} = \mathcal{F}^{-1}\left\{\tilde{L}_m \hat{\overline{K}}_j^e \tilde{P}(k_x, k_y)\tilde{G}_o^+(k_x, k_y)\right\} \tag{6.117}$$

$$L_m F^{ii} = \mathcal{F}^{-1}\left\{\tilde{L}_m \hat{\overline{K}}_i^m \tilde{P}(k_x, k_y)\tilde{G}_o(k_x, k_y)\right\} \tag{6.118}$$

$$L_m \overline{F}^{ij} = \mathcal{F}^{-1}\left\{\tilde{L}_m \hat{\overline{K}}_j^m \tilde{P}(k_x, k_y)\tilde{G}_o^+(k_x, k_y)\right\} \tag{6.119}$$

$$L_m \frac{\partial}{\partial z}\overline{A}^{ij} = (-1)^i \mathcal{F}^{-1}\left\{\tilde{L}_m \hat{\overline{K}}_j^e \tilde{P}(k_x, k_y)\tilde{G}_{oz}^+(k_x, k_y)\right\} \tag{6.120}$$

and

$$L_m \frac{\partial}{\partial z}\overline{F}^{ij} = (-1)^i \mathcal{F}^{-1}\left\{\tilde{L}_m \hat{\overline{K}}_j^m \tilde{P}(k_x, k_y)\tilde{G}_{oz}^+(k_x, k_y)\right\} \tag{6.121}$$

allowing the evaluation of the pertinent integral without a need to generate a square matrix. In (6.116)–(6.121), $\tilde{G}_o(k_x, k_y)$ has already been given in (6.85),

$$\begin{aligned}
\tilde{G}_o^+(k_x, k_y) &= \mathcal{F}\left\{G_o(\overline{r}_1 - \overline{r}_2')\right\} = \mathcal{F}\left\{G_o(\overline{r}_2 - \overline{r}_1')\right\} \\
&= \begin{cases} \frac{1}{2j\sqrt{k_o^2 - k_x^2 - k_y^2}} e^{-j\tau/2\sqrt{k_o^2 - k_x^2 - k_y^2}} & k_x^2 + k_y^2 < k_o^2 \\ \frac{1}{2j\sqrt{k_x^2 + k_y^2 - k_o^2}} e^{-\tau/2\sqrt{k_x^2 + k_y^2 - k_o^2}} & k_x^2 + k_y^2 > k_o^2 \end{cases}
\end{aligned} \tag{6.122}$$

and

$$\tilde{G}_{oz}^{+}(k_x,k_y)=\frac{\partial}{\partial z}\mathcal{F}\left\{G_o(\bar{r}-\bar{r}_1')\right\}_{z=\tau/2}=-\frac{\partial}{\partial z}\mathcal{F}\left\{G_o(\bar{r}-\bar{r}_2')\right\}_{z=0}$$
$$=\begin{cases}-\frac{1}{2}e^{-j\tau/2\sqrt{k_o^2-k_x^2-k_y^2}} & k_x^2+k_y^2<k_o^2\\ -\frac{1}{2}e^{-\tau/2\sqrt{k_x^2+k_y^2-k_o^2}} & k_x^2+k_y^2>k_o^2\end{cases} \tag{6.123}$$

As noted earlier, (6.85), (6.122) and (6.123) are analytically derived continuous transforms. Therefore, to avoid aliasing, in a numerical implementation of (6.114) in conjunction with (6.116)–(6.121) $\tilde{G}_o(k_x,k_y)\tilde{P}(k_x,k_y)$ should be replaced by the transform of its discrete counterpart $g_o(x_m)$ given by (6.86). Also, $\tilde{G}_o^{+}(k_x,k_y)\tilde{P}(k_x,k_y)$ should be replaced by the transform of the discrete function

$$g_o^{+}(x_n,y_m)=\int_{x_n-\frac{\Delta x}{2}}^{x_n+\frac{\Delta x}{2}}\int_{y_m-\frac{\Delta y}{2}}^{y_m+\frac{\Delta y}{2}}\frac{e^{-jk_o\sqrt{x'^2+y'^2+(\tau/2)^2}}}{4\pi\sqrt{x'^2+y'^2+(\tau/2)^2}}dx'dy'$$
$$=\frac{e^{-jk_o\sqrt{\rho_{nm}^2+(\tau/2)^2}}}{4\pi\sqrt{\rho_{nm}^2+(\tau/2)^2}}\Delta x\Delta y \tag{6.124}$$

Likewise $\tilde{G}_{oz}^{+}(k_x,k_y)\tilde{P}(k_x,k_y)$ should be replaced by the transform of the discrete function

$$g_{oz}^{+}(x_n,y_m)=\frac{\partial}{\partial z}\int_{x_n-\frac{\Delta x}{2}}^{x_n+\frac{\Delta x}{2}}\int_{y_m-\frac{\Delta y}{2}}^{y_m+\frac{\Delta y}{2}}\frac{e^{-jk_o\sqrt{x'^2+y'^2+z^2}}}{4\pi\sqrt{x'^2+y'^2+z^2}}dx'dy'\Bigg|_{z=\tau/2}$$
$$=-\frac{\tau}{2}\left(jk_o+\frac{1}{\rho_{nm}^2+(\tau/2)^2}\right)\frac{e^{-jk_o\sqrt{\rho_{nm}^2+(\tau/2)^2}}}{4\pi\sqrt{\rho_{nm}^2+(\tau/2)^2}}\Delta x\Delta y \tag{6.125}$$

6.8 Scattering by a Material Filled Groove

a. Introduction to Higher Order Boundary Conditions

In this section we consider the application of higher order boundary conditions [26, 27] for the simulation of a material filled groove

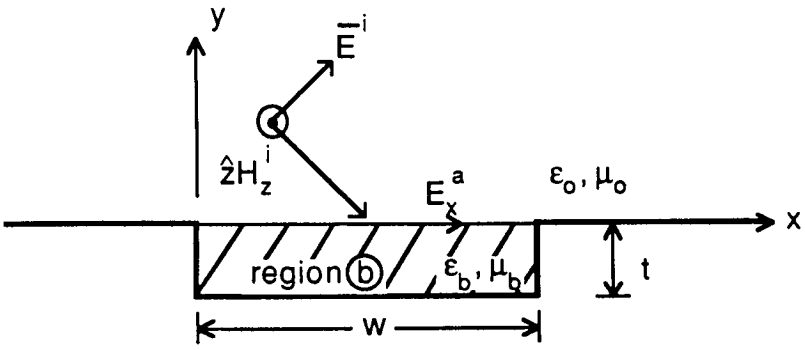

Figure 6.32 Geometry of the rectangular groove in a ground plane.

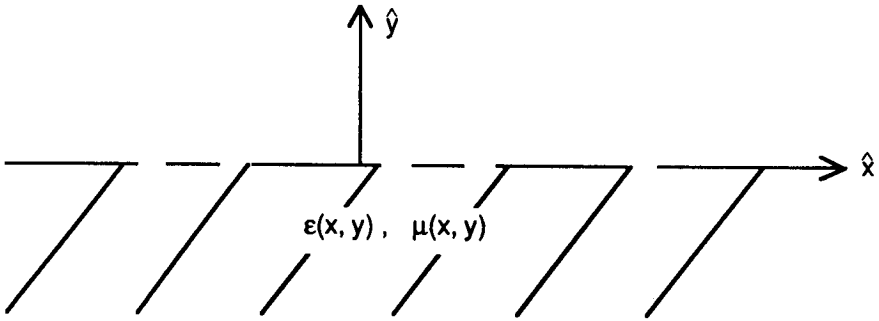

Figure 6.33 Geometry of the profile to be simulated with a boundary condition at $y = 0$.

as shown in Fig. 6.32. Traditional formulations [28] result in integral equations not amenable to a CGFFT solution. In contrast, the application of higher order or generalized impedance boundary conditions (GIBCs) lead to an integral equation that is suited for a CGFFT solution. These involve higher order field derivatives beyond the first and have been found to provide a substantially better simulation for fairly thick dielectric coatings than the standard impedance boundary condition [27, 29].

For a planar surface coincident with the xz plane, as shown in Fig. 6.33, the GIBCs take the form

$$\sum_{m=0}^{M_G} \frac{a_m}{(-jk_o)^m} \frac{\partial^m E_y}{\partial y^m} = 0 \tag{6.126}$$

$$\sum_{m=0}^{M_G} \frac{a'_m}{(-jk_o)^m} \frac{\partial^m H_y}{\partial y^m} = 0 \tag{6.127}$$

where a_m and a'_m are constants specific to the surface of the layer or coating being modeled. On the basis of duality, these cannot be chosen independently and they can be shown [27] to satisfy the relation

$$\left(\sum_{m=0,2,\ldots} a_m\right)\left(\sum_{m=0,2} a'_m\right) = \left(\sum_{m=1,3,\ldots} a_m\right)\left(\sum_{m=1,3,\ldots} a'_m\right) \tag{6.128}$$

The value of M_G determines the order of the conditions, but in practice M_G should be kept as small as possible so that the resulting integral equation is less cumbersome for implementation. When $M_G = 1$, (6.126)–(6.127) reduce to the well known standard impedance boundary condition (SIBC)

$$E_y - \frac{a_1}{jka_o} \frac{\partial E_y}{\partial y} = 0, \qquad H_y - \frac{a_0}{jka_1} \frac{\partial H_y}{\partial y} = 0 \tag{6.129}$$

where $a_1/a_0 = a'_o/a'_1$ in view of (6.128). Using Maxwell's equations (6.129) can also be written in terms of tangential components as

$$\hat{y} \times (\hat{y} \times \overline{E}) = -Z_o \frac{a_0}{a_1} (\hat{y} \times \overline{H}) \tag{6.130}$$

which is a more commonly known form of the SIBC.

b. Higher Order Boundary Conditions for a Metal-Backed Dielectric Layer

In a numerical simulation of the groove in a ground plane, it is of interest to replace its presence with an equivalent boundary condition to be applied at the opening of the groove ($y = 0^+$). Given such a boundary condition, the equivalence principle may be applied

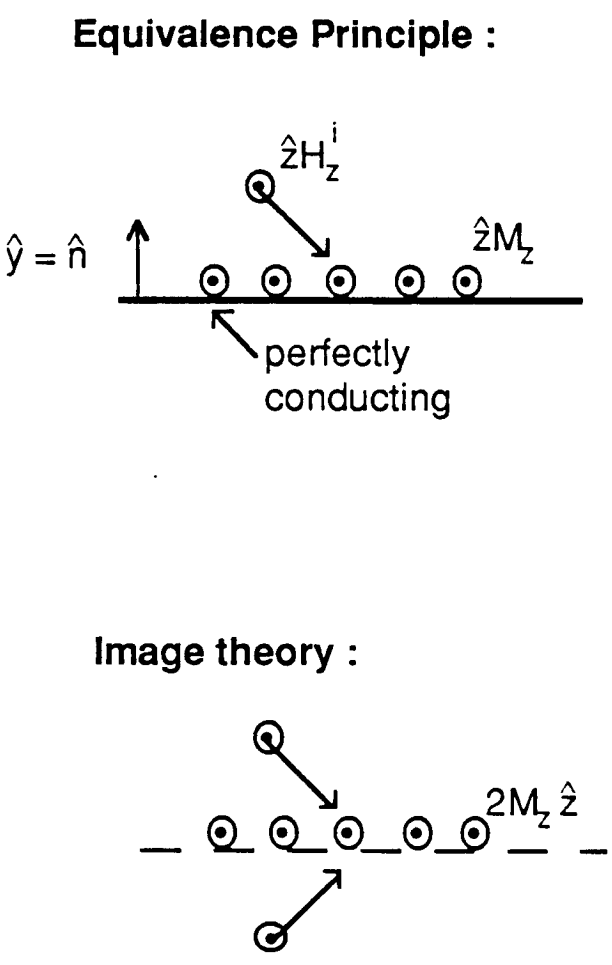

Figure 6.34 Illustration of the application of the equivalance and image theory in the case of a groove in a ground plane.

to extend the ground plane over the groove (see Fig. 6.34) since the fields within the cavity are no longer needed explicitly. A magnetic current may then be introduced satisfying the imposed boundary condition and, subsequently, the ground plane can be removed by invoking image theory.

To find a suitable boundary condition for this purpose, the groove can be thought as a truncated metal-backed dielectric layer. However, since the derivation of boundary conditions accounting for the presence of the specific groove terminations is not possible, we will instead

consider boundary conditions derived for an infinite dielectric coating. Customarily, such a coating is approximately simulated by the SIBC given in (6.129) or (6.130) provided the constants are chosen as

$$\frac{a_0}{a_1} = j\frac{\kappa}{\varepsilon_b}\tan(k_o\kappa t) \tag{6.131}$$

where $\kappa = \sqrt{\varepsilon_b\mu_b}$, ε_b and μ_b are the relative permittivity and permeability of the dielectric layer and t denotes its thickness (depth of the groove). As shown in Fig. 6.35, the SIBC cannot accurately reproduce the reflection coefficients of the coating unless it is of small thickness and/or composed of a high contrast dielectric ($\kappa \gg 1$). The primary reason for this inaccuracy is because the SIBC is not capable of simulating polarization currents normal to the layer and, as a result, is better suited for near normal incidences. However, by increasing the order of the condition, it is possible to permit accurate simulations of fairly thick layers.

A recently derived [27, 29] third order GIBC accomplishes a much better simulation of the dielectric coating. The constants for this GIBC to be placed at the surface of the layer are

$$\begin{aligned}
a_0 &= \left(\kappa - \frac{1}{2\kappa}\right)\left[\tan(kt\kappa) - \tan\left(\frac{kt}{2\kappa}\right)\right] \\
a_1 &= -j\varepsilon_b\left[1 + \tan(kt\kappa) - \tan\left(\frac{kt}{2\kappa}\right)\right] \\
a_2 &= \frac{1}{2\kappa}\left\{\tan(kt\kappa) - \tan\left(\frac{kt}{2\kappa}\right) + kt\left(\kappa - \frac{1}{2\kappa}\right)\right. \\
&\qquad \left.\cdot\left[1 + \tan(kt\kappa)\tan\left(\frac{kt}{2\kappa}\right)\right]\right\} \\
a_3 &= \frac{jkt\varepsilon_b}{2\kappa}\left[\tan(kt\kappa) - \tan\left(\frac{kt}{2\kappa}\right)\right]
\end{aligned} \tag{6.132}$$

and

$$\begin{aligned}
a_0' &= (2\kappa^2 - 1)\left[1 + \cot(kt\kappa)\cot\left(\frac{kt}{2\kappa}\right)\right] \\
a_1' &= -j2\kappa\mu_b\left[\cot(kt\kappa) - \cot\left(\frac{kt}{2\kappa}\right)\right]
\end{aligned}$$

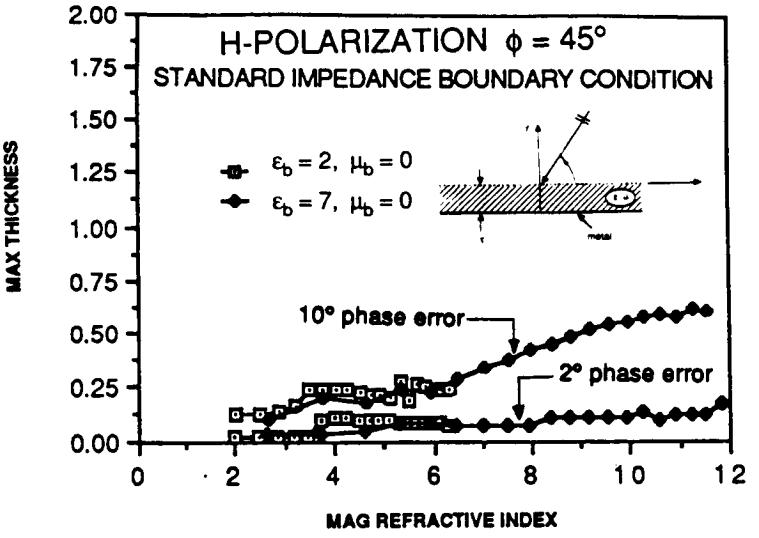

(a)

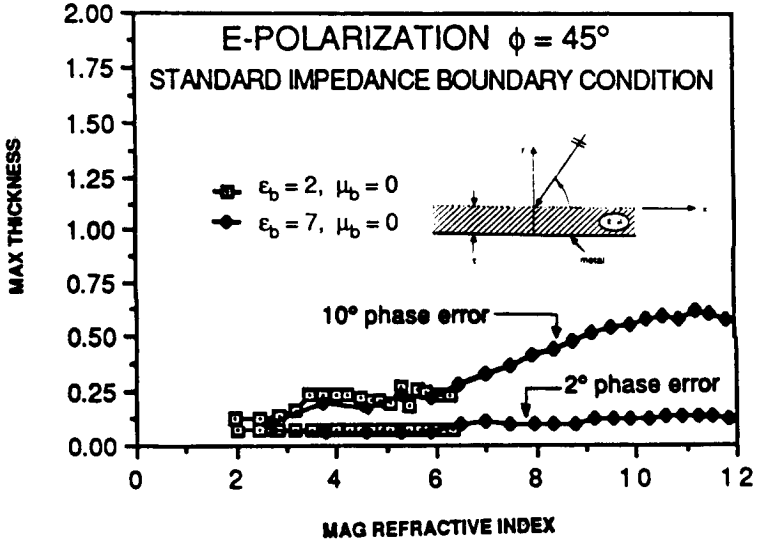

(b)

Figure 6.35 Maximum allowed thickness vs $|\kappa|$ for a metal-backed dielectric layer modelled using the first order (standard impedance) boundary conditions at $y = t+$ with 2-degree and 10-degree phase errors. Curves shown are for $\varepsilon_b = 2$ and $\varepsilon_b = 7$ with $\phi = 45°$: (a) H-polarization, (b) E-polarization.

$$a_2' = 1 + \cot(kt\kappa)\cot\left(\frac{kt}{2\kappa}\right) + kt\left(\kappa - \frac{1}{2\kappa}\right)\left[\cot(kt\kappa) - \cot\left(\frac{kt}{2\kappa}\right)\right]$$

$$a_3' = jkt\mu_b\left[1 + \cot(kt\kappa)\cot\left(\frac{kt}{2\kappa}\right)\right] \tag{6.133}$$

They can be derived by employing a suitable expansion of the coating's Fresnel reflection coefficient compatible with that implied by (6.126)–(6.127) and as shown in Fig. 6.36 they are substantially more accurate than the SIBC. Unlike the SIBC, their accuracy improves as the incidence angle approaches grazing. Also, they become more accurate as the loss in the dielectric increases. Clearly, their limitation for the present application concerns the terminations of the groove/coating not accounted in the derivation of (6.132)–(6.133). This is rarely addressed in applications involving the SIBC but becomes a more important issue when dealing with higher order boundary conditions because of their inherent non-uniqueness at abrupt terminations. That is, the GIBCs require supplemental conditions specifying the termination's geometry across its depth. Before, however, we address corrective measures relating to this difficulty, let us first examine a direct implementation of the GIBC as applied to the simulation of the groove.

c. Formulation of Integral Equations Using GIBCs

Consider an illumination of the groove in Fig. 6.32 by the H-polarized plane wave given in (6.41)–(6.42). For this case, $H_y = 0$, and thus the relevant GIBC is (6.126). Expanding this for $M_G = 3$ we have

$$\left(a_0 - \frac{a_2}{k_0^2}\frac{\partial 2}{\partial y^2}\right)E_y + \left(-\frac{a_1}{jk_o} + \frac{a_3}{jk_o^3}\frac{\partial^2}{\partial y^2}\right)\frac{\partial E_y}{\partial y} = 0; \quad y = 0^+, 0 < x < w \tag{6.134}$$

Referring now to Fig. 6.34 we may introduce the equivalent magnetic currents $\overline{M} = \overline{E} \times \hat{y} = \hat{z}E_z$ in (6.134). To do so, we note that since

$$\nabla \cdot \overline{E} = 0$$

we have

$$\frac{\partial E_y}{\partial y} = -\frac{\partial E_x}{\partial x} = -\frac{\partial M_z}{\partial x} \tag{6.135}$$

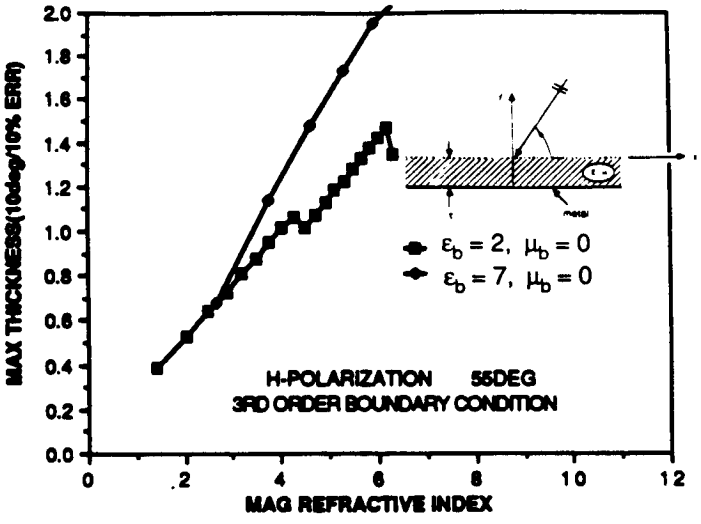

(a)

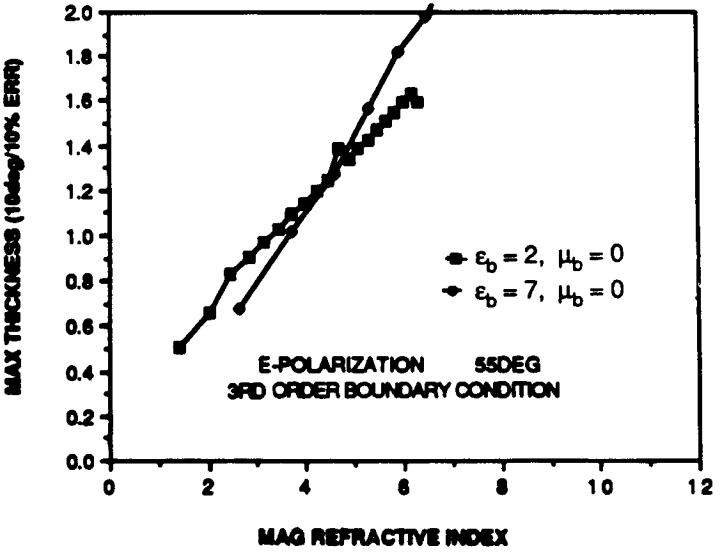

Figure 6.36 Maximum allowed thickness vs $|\kappa|$ for a metal-backed layer modelled using third order GIBC with a 10-degree phase (and/or 10 percent amplitude) error. Curves shown are for $\varepsilon_b = 2$ and $\varepsilon_b = 7$ with incidence at 55° from grazing (a) H-polarization, (b) E-polarization.

Substituting (6.135) into (6.134) yields

$$\begin{aligned}&\frac{j}{4}\left[a_0+\frac{a_2}{k_0^2}\left(k_0^2+\frac{\partial^2}{\partial x^2}\right)\right]\int_0^w 2M_z(x')\frac{\partial}{\partial x}H_0^{(2)}(k_o|x-x'|)dx'\\&+\frac{1}{jk_o}\left[a_1+\frac{a_3}{k_0^2}\left(k_0^2+\frac{\partial^2}{\partial x^2}\right)\right]\frac{\partial M_z(x)}{\partial x}\\&=\left(a_0-\frac{a_2}{k_0^2}\frac{\partial^2}{\partial y^2}\right)2Z_o\cos\phi_o H_z^i\end{aligned}\tag{6.136}$$

and in deriving this we have also employed the wave equation

$$\frac{\partial^2 E_y}{\partial y^2}=-\frac{\partial^2 E_y}{\partial x^2}-k_0^2E_y\tag{6.137}$$

to change even derivatives with respect to y to corresponding derivatives with respect to x. Further, we have set

$$E_y=E_y^i+E_y^r+E_y^s=2Z_o\cos\phi_o H_z^i+E_y^s\tag{6.138}$$

where

$$E_y^s=-\frac{j}{4}\int_0^w 2M_z(x')H_0^{(2)}(k_o|x-x'|)dx'\tag{6.139}$$

is the y component of the scattered field in which the factor of 2 is due to image theory.

The integral equation (6.136) can be simplified further by integrating both sides with respect to x to eliminate one of the derivatives. Doing so yields

$$\begin{aligned}&\left[1+\frac{a_2}{a_0}\left(1+\frac{1}{k_0^2}\frac{\partial^2}{\partial x^2}\right)\right]\frac{k_oY_o}{2}\int_0^w M_z(x')H_0^{(2)}(k_0|x-x'|)dx'\\&+\left[\frac{a_1}{a_0}+\frac{a_3}{a_0}\left(1+\frac{1}{k_0^2}\frac{\partial^2}{\partial x^2}\right)\right]Y_oM_z(x)\\&=2\left[1+\frac{a_2}{a_0}\left(1+\frac{1}{k_0^2}\frac{\partial^2}{\partial x^2}\right)\right]e^{jk_o(x-w/2)\cos\phi_o}\end{aligned}\tag{6.140}$$

By employing the Fourier transform to evaluate the convolution integrals, this may now be written as

$$\frac{k_o}{2}\mathcal{F}^{-1}\left[\hat{g}_1\hat{M}_z\right] + \frac{a_2}{a_o}\frac{1}{2k_o}\mathcal{F}^{-1}\left[\left(k_o^2 - k_x^2\right)\hat{g}_1\hat{M}_z\right] + \frac{a_1}{2a_o}M_z(x) + \frac{a_3}{2k_o^2 a_o}\mathcal{F}^{-1}\left[\left(k_o^2 - k_x^2\right)\hat{M}_z\right] = 2z_o\left(1 + \frac{a_2}{a_o}\sin^2\phi_o\right)e^{jk_o\left(x-\frac{w}{2}\right)\cos\phi_o} \tag{6.141}$$

where $\hat{g}_1$ is the discrete Fourier transform of $g_1(x_n)$ given in (6.53) and $\hat{M}_z$ denotes the transform of the sample train representing $M_z(x)$. An implementation of (6.141) via the CGFFT method is a straightforward task. In contrast, a corresponding implementation of (6.140) via the MoM could have resulted in numerical difficulties because of the presence of the higher order derivatives in addition to having a $O(N^2)$ memory demand.

Typical results of the current and scattering as computed via a CGFFT solution of (6.141) are compared with exact data in Fig. 6.37 for a $\lambda_o/5$ deep groove of width $w = 1\lambda_o$. As expected, the solution based on the third order GIBC predicts the magnitude and phase of the current distribution reasonably well away from the groove terminations. This, of course, is the cause of the discrepancies in the scattering patterns, particularly, for near grazing incidence. Corresponding results based on the SIBC are shown in Fig. 6.38. In contrast to the GIBC results, the current distribution based on the SIBC represents only an average value of the actual distribution.

d. Hybrid GIBC — Exact Formulation

The GIBC formulation in conjunction with the CGFFT solution method offers the advantage of having an O(N) memory requirement. However, as seen in Fig. 6.37, the current distribution predicted by the third order GIBC is not of acceptable accuracy when within 0.2 wavelengths of the groove terminations or so. To alleviate this difficulty, one approach is to feed the currents predicted by the GIBC integral equation (141) away from the edges into the exact integral equation [30]. The last can then be solved for the remaining currents in the vicinity of the groove terminations. This only requires the inversion of a small matrix, thus alleviating the usual storage difficulties, particularly when considering a three-dimensional application.

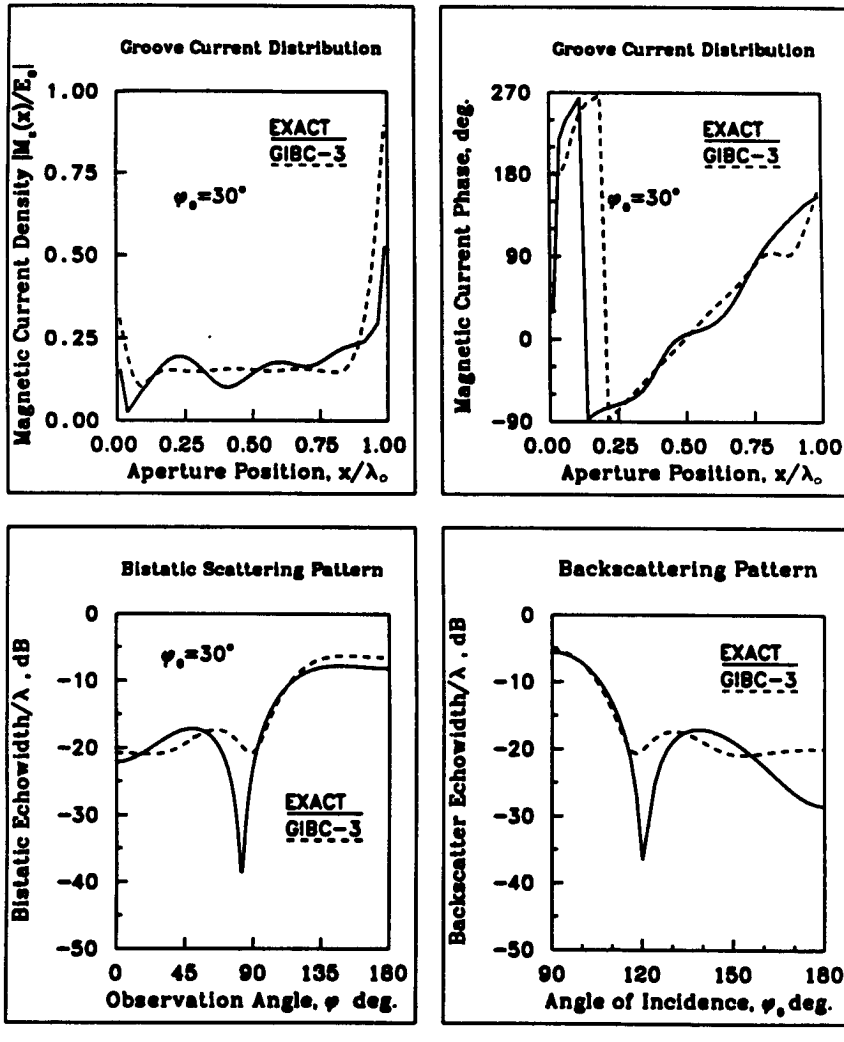

Figure 6.37 Scattering by a groove in a ground plane; comparison of the exact and third order GIBC solutions for a groove of width $w = 1\lambda_o$, depth $t = 0.2\lambda_o$, $\varepsilon_b = 7.0 - j1.0$, and $\mu_b = 1$.

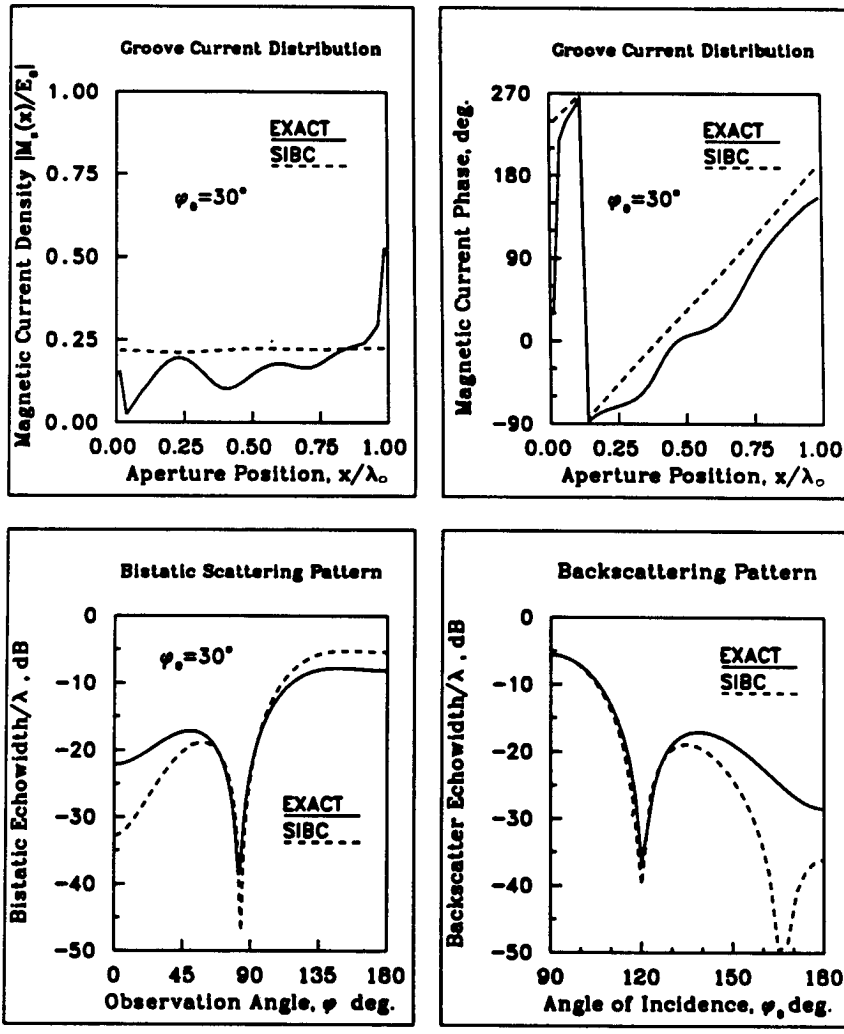

Figure 6.38 Scattering by a groove in a ground plane; comparison of the exact and SIBC solutions for a groove of width $w = 1\lambda_o$, depth $t = 0.2\lambda_o$, $\epsilon_b = 7.0 - j1.0$, and $\mu_b = 1$.

The exact integral equation for the equivalent magnetic currents is

$$2e^{jk_o(x-w/2)\cos\phi_o} - \frac{k_oY_o}{2}\int_0^w M_z(x')H_0^{(2)}(k_o|x-x'|)dx' = -jk_bY_b\int_0^w M_z(x')G_b(x,x')dx' \tag{6.142}$$

where

$$G_b(x,x') = \sum_{p=0}^{\infty}\frac{\varepsilon_p}{wk_p\tan(k_pt)}\cos\left(\frac{p\pi x'}{w}\right)\cos\left(\frac{p\pi x}{w}\right) \tag{6.143}$$

is the Green's function for the cavity,

$$Y_b = \frac{1}{Z_b} = -\frac{j\varepsilon_bY_o}{\kappa\tan(k_o\kappa t)} = \frac{a_o}{a_1} \tag{6.144}$$

$$\varepsilon_p = \begin{cases} 1 & p=0 \\ 2 & p>0 \end{cases} \tag{6.145}$$

and

$$k_p = \sqrt{k_0^2\varepsilon_b\mu_b - \left(\frac{p\pi}{w}\right)^2} \tag{6.146}$$

Suppose now that $M_z^G(x)$ denotes the current computed via the GIBC integral equation (6.141). Employing $M_z^G(x)$ in place of $M_z(x)$ in (6.142) for $x_\Delta < x < w - x_\Delta$ we may then write

$$M_z(x) = \begin{cases} M_z^G(x) & x_\Delta < x < w - x_\Delta \\ M_z^e(x) & 0 < x < x_\Delta, w - x_\Delta < x < w \end{cases} \tag{6.147}$$

and when this is substituted into (6.142) yields

$$\begin{aligned} 2e^{jk_o(x-w/2)\cos\phi_o} &+ \int_{x_\Delta}^{w-x_\Delta} M_z^G(x')\left[jk_oY_bG_b(x,x') - \frac{k_oY_o}{2}H_o^{(2)}(k_o|x-x'|)\right]dx' \\ &= -\int_0^{x_\Delta} M_z^e(x')\left[jk_bY_bG_b(x,x') - \frac{k_oY_o}{2}H_o^{(2)}(k_o|x-x'|)\right]dx' \\ &\quad - \int_{w-x_\Delta}^{w} M_z^e(x')\left[jk_bY_bG_b(x,x') - \frac{k_oY_o}{2}H_0^{(2)}(k_o|x-x'|)\right]dx' \end{aligned} \tag{6.148}$$

Assuming that $M_z^G(x)$ has already been computed via a CGFFT solution of (6.141), the entire left-hand side of (6.148) is known. Thus, for $x_\Delta < 0.25$, a 4×4 or a 6×6 square admittance matrix is required for the solution of $M_z^e(x)$. In general, continuity of the current density must be imposed at the transition regions between $M_z^G(x)$ and $M_z^e(x)$, and this can be accomplished through simple averaging.

The results presented in Fig. 6.39 clearly show that the proposed hybrid formulation can provide an accurate prediction of the current and scattering associated with the groove. Additional backscatter data which provide a testament to the conclusion are given in Fig. 6.40. The depth of the chosen groove corresponding to the patterns in Fig. 6.40 is $0.4\lambda_o$ and it is seen that the GIBC-exact hybrid solution (HYBRID-3) is still in good agreement with the exact. In contrast, the SIBC or SIBC-exact hybrid (HYBRID-1) solutions do not provide an acceptable accuracy near edge-on incidences. As stated earlier, this is due to the limited accuracy of the SIBC.

6.9 Additional Improvements in the Implementation of the CGFFT Solution Algorithm

a. Differentiation in the spatial domain

In all applications of the CGFFT solution it was noted that the FFT played a major role in the accuracy and convergence of the solution. In particular, two issues were of crucial importance, both of which were related to the discretization of the original continuous system. One issue dealt with aliasing errors caused by the truncation of the infinite domain associated with the continuous transform of the Green's function. Another dealt with errors because of differences between the transforms of the continuous function and its sample train. The last was corrected by an explicit introduction of a basis function as is usually done with MoM solutions. A corrective process was also discussed to eliminate aliasing errors by discretizing the integral equation before application of the FFT. This eliminates the need to deal with the infinite domain Green's function replacing it with a discrete function of finite duration which can be treated as a periodic function, thus eliminating aliasing.

A general rule in improving the convergence of the CGFFT solution algorithm is to reduce the spectral content of the functions handled

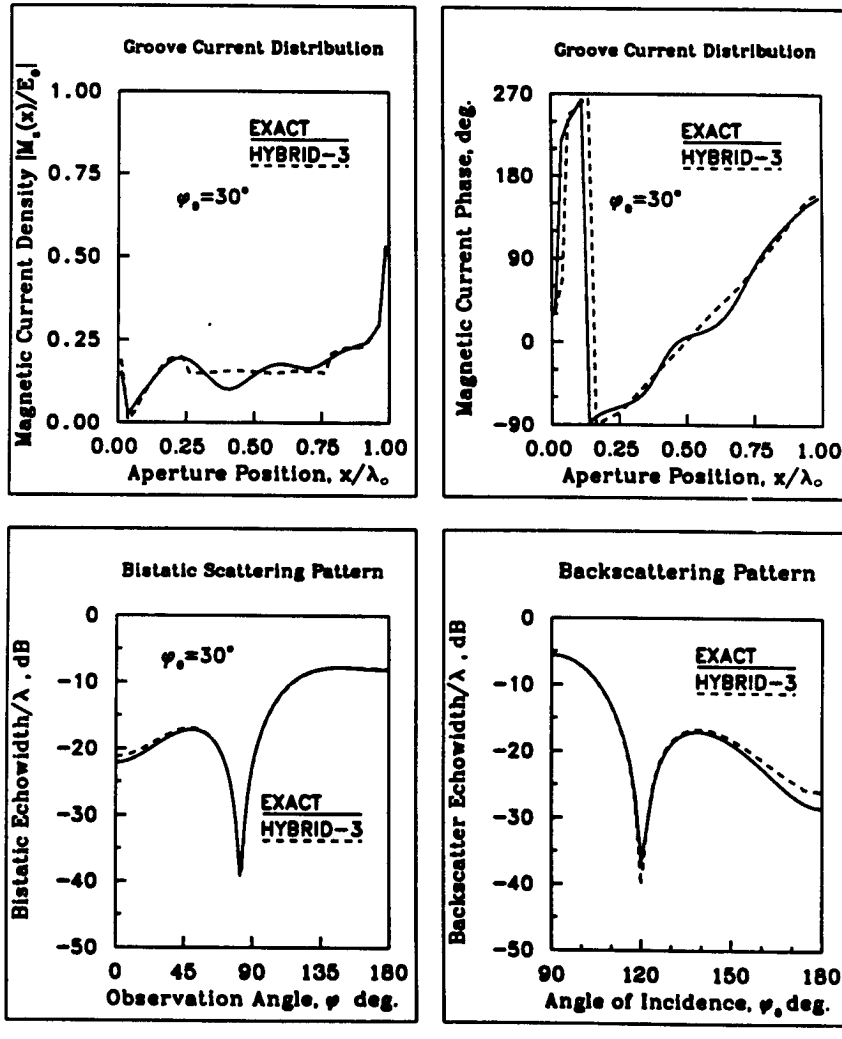

Figure 6.39 Scattering by a groove in a ground plane; comparison of exact and hybrid GIBC solutions for a groove of width $w = 1\lambda_o$, depth $t = 0.2\lambda_o$, $\varepsilon_b = 7.0 - j1.0$ and $\mu_b = 1$.

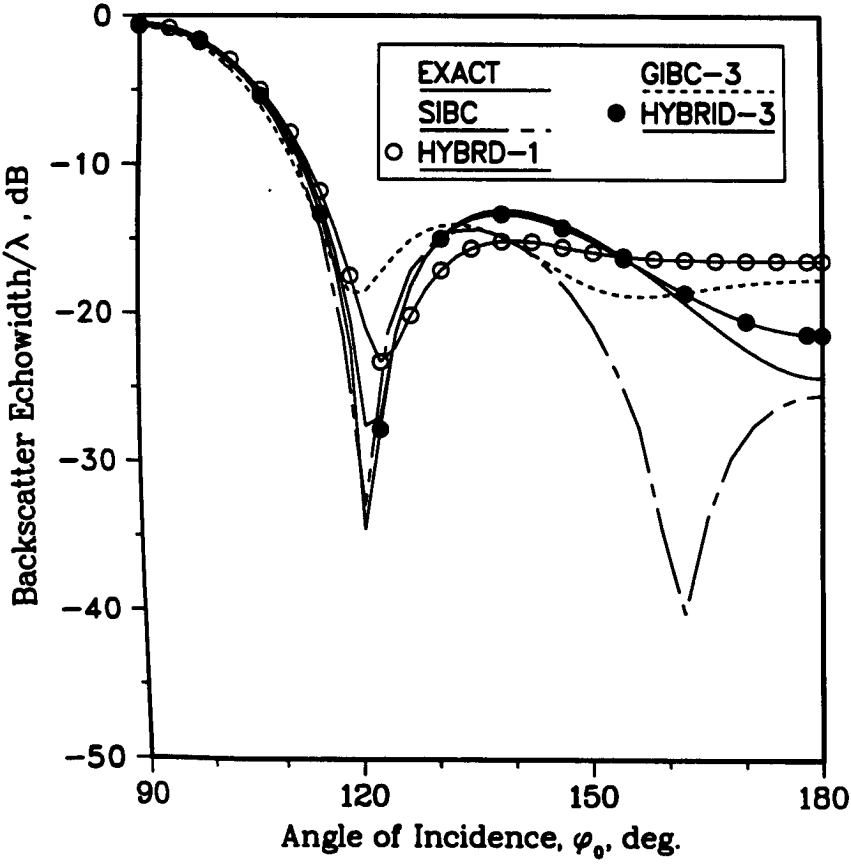

Figure 6.40 Comparison of backscattering pattern obtained by the indicated formulations for a groove having $w = 1\lambda_o$, $t = 0.4\lambda_o$, $\varepsilon_b = 7.0 - j1.0$, and $\mu_b = 1$.

by the FFT. The quantities forming the convolution integral must, of course, be treated in the spectral domain to realize the memory advantage. However, the usual presence of derivatives increases the spectral content of the transformed quantities if carried under the integral. This is observed in the systems (6.45), (6.64)–(6.66), (6.82)–(6.85), and (6.87). The replacement of the continuous derivative with a discrete, as suggested by (6.56), introduces an envelope that acts as a filter to reduce the effect of high frequency components. An alternative is to handle the derivatives in the spatial domain. For example, (6.87) may be instead written as

$$\begin{aligned} RK_x^e + \frac{c_o Z_o}{\Delta^2}\left[D_1 \mathcal{F}^{-1}\left\{\hat{K}_x^e \hat{g}_o\right\} + D_2 \mathcal{F}^{-1}\left\{\hat{K}_y \hat{g}_o\right\}\right] &= E_x^i \\ RK_y^e + \frac{c_o Z_o}{\Delta^2}\left[D_2 \mathcal{F}^{-1}\left\{\hat{K}_x^e \hat{g}_o\right\} + D_3 \mathcal{F}^{-1}\left\{\hat{K}_y \hat{g}_o\right\}\right] &= E_y^i \end{aligned} \tag{6.149}$$

where $\Delta = \Delta x = \Delta y$ and D_i are the discrete representations of the operators $\Delta^2 L_i$. To $O(\Delta^2)$ these can be approximated using center difference formulas as

$$\begin{aligned} D_1 s_{n,m} &= \Delta^2 L_1 s_{n,m} = s_{n+1,m} + (k_o^2\Delta^2 - 2)s_{n,m} + s_{n-1,m} \\ D_2 s_{n,m} &= \Delta^2 L_2 s_{n,m} = \frac{1}{4}(s_{n+1,m+1} - s_{n-1,m+1} \\ &\quad + s_{n-1,m-1} - s_{n+1,m-1}) \end{aligned} \tag{6.150}$$

The discrete forms of the remaining operators defined in (6.81) can be written in a similar manner. We have,

$$\begin{aligned} D_3 s_{n,m} &= \Delta^2 L_3 s_{n,m} = s_{n,m+1} + (k_o^2\Delta^2 - 2)s_{n,m} + s_{n,m-1} + O(\Delta^2) \\ D_4 s_{n,m} &= \Delta^2 L_4 s_{n,m} = s_{n+1,m} + s_{n,m+1} - 4s_{n,m} + s_{n-1,m} + s_{n,m-1} \\ D_5 s_{n,m} &= 2\Delta L_5 s_{n,m} = s_{n+1,m} - s_{n-1,m} \\ D_6 s_{n,m} &= 2\Delta L_6 s_{n,m} = s_{n,m+1} - s_{n,m-1} \end{aligned} \tag{6.151}$$

A drawback in using (6.150)–(6.151) is the additional arithmetic operations required for their implementation versus the simple multiplication that could be performed if the derivative operations were carried under the integral to be evaluated via the FFT. One should, of course, make the appropriate choice based on the advantages offered by each process. That is, implementation of the differential operators

should be done in the spatial domain as dictated by (6.150)–(6.181) provided the time required for the additional arithmetic operations is outweighed by the improved convergence rate. Otherwise, they should be implemented as noted in the previous sections.

b. Vector and parallel implementation of the CGFFT algorithm

Most modern computing facilities now offer vector and parallel processing capabilities. A vector facility exploits the independence of operations, particularly those associated with the elements in an array/vector. A typical example of vectorization occurs when performing addition or the Hadamard product of two independent arrays/vectors. In a scalar machine, each element product or addition will be done sequentially, whereas in a vector facility vector registers are employed to perform several of the element operations concurrently. That is, when a DO loop is encountered, the loop iterations are not executed sequentially but in parallel provided there is no data dependences among the loop iterations. When a parallel (concurrent) facility is also available, independent operations or sections of the program may be executed on different processors. In this manner, several matrix operations involving independent vectors/arrays may be performed in parallel. Typically, a vector instruction is capable of handling 32 to 128 data elements at once resulting in a two to four times increase in the execution time.

The CGFFT algorithm lends itself to vectorization and parallel processing. Most operations involve array manipulations which are vectorizable. Also, several of the steps in the iteration algorithm can be treated independently and can thus be performed on different processors. Most importantly, since the FFT is a highly vectorizable algorithm, it plays a major role in the speed of the solution algorithm and overall efficiency of the optimized code.

To demonstrate the speed advantage which can be realized when executing the CGFFT solution on a vector-concurrent facility, a few tests were performed on the Alliant FX/8 and the IBM 3090-600E. The Alliant used in this study has four vector processors (expandable to 8), 56 Mbytes of main memory and 256 Kbytes of cache memory with a bus capable of handling 188 Mbytes per second. The IBM 3090-600E supercomputer has six processors, 256 Mbytes of real memory and 64 Kbytes of cache memory for each processor. Also, both machines offer an optimized vectorized radix 2 FFT routine.

CGFFT Code Performance	Scalar (scalar FFT)	Vector (scalar FFT)	Vector (vector FFT)
ELAPSED CPU, sec	148	129	34
VECTOR CPU, sec	-	9	30
VECTORIZABLE CODE, sec	-	28	144
VECTOR CONTENT	-	18.9%	97.3%
VECTOR SPEED UP	-	3.1	4.8
PROGRAM SPEED UP	-	1.15	4.35

Table 6.1 Performance of the scalar and vectorized 3-D code on the IBM 3090.

Tables 6.1 and 6.2 show the performance of the CGFFT algorithm executed on the Alliant and IBM vector facilities for computing the currents on a $2\lambda_o \times 2\lambda_o$ plate. It is clear from Table 6.1 that the majority of the speed-up in the execution time for the IBM is attributed to the vectorized FFT leading to an overall speed-up over 400 percent. In the case of the Alliant, the overall speed-up was more than 600 percent per iteration. The speed-up in execution time is even more impressive when all four processors of the Alliant are utilized. As seen from Table 6.3, the speed-up when using the four processors is 3.5 times that over the single. This implies a speed-up of more than 20 times per iteration when combined with the data in Table 6.2. Interestingly, similar speed-ups are observed for larger plates indicating that the aforementioned results are independent of the cache memory [31].

Additional improvements in the execution speed of the FFT may be realized by employing a prime factor FFT [15, 32–36]. Traditional radix-2 FFTs are restricted to sizes which coincide with powers of 2. As noted earlier, when employing the FFT in the CG solution method, it is not necessary to choose an FFT size/pad more than twice the size of the geometry. Therefore, the restriction associated with base-2 FFTs

CGFFT Code Performance	Scalar (scalar FFT)	Vector (scalar FFT)	Vector (vector FFT)
INITIALIZATION, sec	2.39	0.72	0.80
CGFFT LOOP, sec	4307.0	1255.2	342.8
TOTAL CPU TIME, sec	4309.3	1255.9	343.6
ITERATIONS	111	111	59
PER ITERATION, sec	38.80	11.31	5.8
MEGAFLOPS	0.0527	0.1807	0.3512
PROGRAM SPEED UP	-	3.43	12.54
SPEED UP/ITERATION	-	3.43	6.69

Table 6.2 Performance of the scalar and vectorized 3-D code on the Alliant FX/8.

will in most cases lead to additional storage and CPU time demand. A prime factor FFT alleviates this restriction since its size can be chosen with more arbitrariness without speed compromises. Although the prime factor FFT does not indeed allow a complete arbitrariness in size, it does allow a finer incrementation in size than the radix-2 FFT. In general, one must be able to express the chosen size as a product of prime factors. For example, the prime factors of 30 are 2, 3, and 5. This allows the 30 point FFT to be written using 2 point, 3 point, and 5 point DFT modules requiring $O(N)$ operations as is the case with the radix-2 FFT.

A further reduction in the execution time of the CGFFT algorithm may be achieved by employing special purpose FFTs which exploit the zero padding of the current distribution. This introduces a substantial amount of multiplications with zeros which can be eliminated a priori

Optimized CGFFT	NO. of processors			
Performance	1	2	3	4
INITIALIZATION, sec	1.60	0.86	0.61	0.50
CGFFT LOOP, sec	407.4	211.0	146.7	115.6
TOTAL CPU TIME, sec	409.0	211.8	147.3	116.1
ITERATIONS	59	59	59	59
PER ITERATION, sec	6.91	3.58	2.49	1.96
MEGAFLOPS	0.2951	0.5697	0.8192	1.0340
SPEED UP	-	1.93	2.78	3.52
EFFICIENCY	-	96.5%	92.7%	88.0%

Table 6.3 FX/8 Vector-Concurrent performance for a $2\lambda_o \times 2\lambda_o$ plate.

to increase the speed of the algorithm as discussed in [15]. It is not clear, however, whether such a special FFT algorithm can be vectorized as effectively as the traditional one. In that case, the use of special purpose FFT algorithms is not recommended. The same also holds for the use of prime factor FFTs. That is, the use of a highly vectorizable FFT algorithm translates into a substantial time savings in the execution of the CG algorithm and may, thus, overcome any advantages offered by special purpose FFTs.

6.10 Concluding Remarks

The theoretical and computational aspects related to the application of the CGFFT method to problems of radiation and scattering are established and well understood. Beyond the basic applications

considered in this chapter, the extension to three dimensional dielectric bodies [25, 36] with and without anisotropy is straightforward by employing the three dimensional FFT. Also, the CGFFT method is directly applicable in solving systems relating to scattering, transmission and radiation by periodic structures and arrays [38–42]. In that case, the resulting system is discrete and no need arises for corrective measures due to discretization.

The main advantage of the CGFFT method is its reduced memory demand in comparison with matrix inversion techniques. For backscatter computations, however, the method becomes computationally intensive and time consuming since the entire solution process must be repeated for each excitation. Speeding-up of the algorithm or solution process will be an integral part of future research in this area, particularly in dealing with three dimensional applications. In this respect, a possible approach, where the scattering pattern due to a given incidence is found as a linear composition of those patterns corresponding to a few special excitations (basis) [43], may prove useful. Most certainly, vectorization and parallelization of the underlying algorithms will be of great importance in reducing the computation time and improving the efficiency of the CGFFT solution method. New emerging methodologies which combine the CGFFT with other numerical techniques will also play roles in this respect. For example, the Finite Element and CGFFT methods can be combined [44,45] to reduce the dimensionality of the required FFT and consequently improve the efficiency of the solution process. In general, hybrid methodologies will likely prevail in overcoming restraints dealing with the computational efficiency and versatility of the iterative solution methods.

References

[1] Hestenes, M. R., and E. Steifel, "Method of Conjugate Gradients for solving linear systems," *J. Res. Nat. Bur. Standard.*, **49, 6**, 409–436, Dec. 1952.

[2] Hestenes, M. R., *Conjugate Direction Methods in Optimization*, New York: Springer-Verlag, 1980.

[3] Strang, G., *Introduction to Applied Mathematics*, Cambridge,

Mass.: Wellesley-Cambridge, 1980.

[4] Brigham, E. O., *The Fast Fourier Transform and its Applications*, Englewood Cliffs, New Jersey: Prentice Hall, 1988.

[5] Sarkar, T. K., E. Arvas, and S. M. Rao, "Application of FFT and the Conjugate Gradient method for the solution of electromagnetic radiation from electrically large and small conducting bodies," *IEEE Trans. Antennas Propagat.*, **AP-34**, 635–640, May 1986.

[6] Bojarski, N. N., "k-Space formulation of the electromagnetic scattering problem" *Tech. Report*, **AFAL-TR-71-5**, Mar. 1971.

[7] van den Berg, P. M., "Iterative computational techniques in scattering based upon the integrated square error criterion," *IEEE Trans. Antennas Propagat.*, **AP-32, 10**, 1063–1071, Oct. 1984.

[8] Borup, D., and O. P. Gandhi, "Fast Fourier Transform method for calculation of SAR distributed in finely discretized inhomogeneous models of biological bodies," *IEEE Trans. Microwave Theory Tech.*, **MTT-32**, Apr. 1984.

[9] Peterson, A. F., "An analysis of the spectral iterative techniques for electromagnetic scattering from individual and periodic structures," *Electromagnetics*, **6**, 255–276, 1986.

[10] Christodoulou, C. G., and J. F. Kaufman, "On the electromagnetic scattering from infinite rectangular grids with finite conductivity," *IEEE Trans. Antennas Propagat.*, **AP-34**, 144–154, Feb. 1986.

[11] Peters, T. J., and J. L. Volakis, "Application of a Conjugate Gradient FFT method to scattering from thin planar material plates," *IEEE Trans. Antennas Propagat.*, **AP-36**, 518–526, Apr. 1988.

[12] Barkeshli, K., and J. L. Volakis, "Improving the convergence rate of the CGFFT method using subdomain basis functions," *IEEE Trans. Antennas and Propagat.*, **AP-37**, 893–900, July 1989.

[13] Shen, C. Y., K. J. Glover, M. I. Sancer, and A. D. Varvatsis, "The Discrete Fourier Transform method of solving differential-integral equations in scattering theory," *IEEE Trans. Antennas and Propagat.*, **AP-37**, 1032–1040, Aug. 1989.

[14] Catedra, M. F., J. G. Cuevas, and L. Nuno, "A scheme to analyze conducting plates of resonant size using the Conjugate Gradient

method and the Fast Fourier Transform," *IEEE Trans. Antennas and Propagat.*, **AP-36**, 1744–1752, Dec. 1988.

[15] Peters, T. J., and J. L. Volakis, "On the formulation and implementation of a Conjugate Gradient FFT method," *Journal of Electromagnetic Waves and Applications*, **3**, **8**, 675–696, 1989.

[16] Bokhari, S. A., and N. Balakrishnan, "A method to extend the spectral iteration technique," *IEEE Trans. Antennas Propagat.*, **AP-34**, 51–57, Jan. 1986.

[17] Harrington, R. F., *Field Computation by Moment Methods*, Malabay, Florida: R. E. Krieger Publishing Co., 1968.

[18] Richmond, J. H., "Radiation and scattering by thin wire structures in a homogeneous conducting medium," *IEEE Trans. Antennas and Propagat.*, 365, Mar. 1974.

[19] Stutzman, W. L., and G. A. Thiele, *Antenna Theory and Design*, New York: John Wiley, ch. 7, 1981.

[20] Senior, T. B. A., "Combined resistive and conductive sheets," *IEEE Trans. Antennas and Propagat.*, **AP-33**, 577–579, May 1985.

[21] Harrington, R. F., *Time Harmonic Electromagnetic Fields*, New York: McGraw Hill, 1969.

[22] Ricoy, M. A., S. A. Kilberg, and J. L. Volakis, "Simple integral equations for two-dimensional scattering with further reduction in unknowns," *IEE Proceeding-H*, **136**, 298–304, Aug. 1989.

[23] Newman, E., and D. M. Pozar, "Electromagnetic modelling of composite wire and surface geometries," *IEEE Trans. Antennas and Propagat.*, **AP-26**, 784–789, Nov. 1978.

[24] Haupt, R., and V. V. Liepa, "Synthesis of tapered resistive strips," *IEEE Trans. Antennas and Propagat.*, **AP-35**, 1217–1225, Nov. 1987.

[25] Peters, T. J., "Computation of the Scattering by Planar and Non-Planar Plates Using a Conjugate Gradient-FFT method," Ph.D. Dissertation, Univ. of Michigan, Ann Arbor, MI, 1988.

[26] Karp, S. N., and L. Karel, Jr., "Generalized impedance boundary conditions with application to surface wave structures," *Electromagnetic Wave Theory*, 479–483, Permagon: New York, 1965.

[27] Senior, T. B. A., and J. L. Volakis, "Derivation and application of a

class of generalized boundary conditions," *IEEE Trans. Antennas and Propagat.*, **AP-37**, 1566–1572, Dec. 1989.

[28] Harrington, R. F., and J. R. Mautz, "A generalized network formulation for aperture problems," *IEEE Trans. Antennas and Propagat.*, **AP-24**, 870–873, Nov. 1976.

[29] Volakis, J. L., T. B. A. Senior, and J. M. Jin, "Derivation and application of a class of generalized boundary conditions – II," *Univ. of Michigan Radiation Laboratory Tech. Report.*, **025921-T-1**, prepared under NASA grant NAG-2-541, Feb. 1989.

[30] Barkeshli, K., and J. L. Volakis, "TE scattering by a two dimensional groove in a ground plane," *IEEE Trans. Antennas and Propagat.*, **AP-38**, 1421–1428, Sept. 1990.

[31] Barkeshli, K., and J. L. Volakis, "A vector concurrent application of a Conjugate Gradient FFT algorithm to electromagnetic radiation and scattering problems," *IEEE Trans. on Magnetics*, **25**, 2892–2894, July 1989.

[32] Temperton, C., "Implementation of a self-sorting in-place prime factor FFT algorithm," *J. Comput. Phys.*, **58**, 283–299, 1985.

[33] Rothweiler, J. H., "Implementation of the in-order prime factor transform for variable sizes," *IEEE Trans. Acoust., Speech, Signal Processing*, **ASSP-30**, **1**, 105–107, Aug. 1982.

[34] Burrus, C. S., and P. W. Eschenbacher, "An in-place, in-order prime factor FFT algorithm," *IEEE Trans. Acoust., Speech, Signal Processing*, **ASSP-29**, **4**, 806–817, Aug. 1981.

[35] Johnson, H. W., and C. S. Burrus, "Large DFT Modules: 11, 13, 17, 19 and 25," *Technical Report No. 8105*, Department of Electrical Engineering, Rice University, Houston, Texas, 1981.

[36] Cátedra, M. F., E. Gago, and L. Naño, "A numerical scheme to obtain the RCS of three dimensional bodies of resonant size using the Conjugate Gradient method and FFT," *IEEE Trans. Antennas and Propagat.*, **AP-37**, 528–537, May 1989.

[37] Su, C-C., "Electromagnetic scattering by a dielectric body with arbitrary inhomogeneity and anisotropy," *IEEE Trans. Antennas and Propagat.*, **AP-37**, 384–389, Mar. 1989.

[38] Peterson, A. F., and R. Mittra, "Iterative-based computational

methods for electromagnetic scattering from individual or periodic structures," *IEEE J. Oceanic Engineering*, **OE-12**, 458–465, Apr. 1987.

[39] Chan, C. H., "Investigation of Iterative and Spectral Galerkin Techniques for solving Electromagnetic Boundary Value Problems," Ph.D. Dissertation, Univ. of Illinois, Urbana, 1987.

[40] Chan, C. H., and R. Mittra, "Some recent developments in iterative techniques for solving electromagnetic boundary value problems," *Radio Sci.*, **22,6**, 929–934, Nov. 1987.

[41] Jin, J. M., and J. L. Volakis, "Electromagnetic scattering by a perfectly conducting patch array on a dielectric slab," *IEEE Trans. Antennas and Propagat.*, **AP-38**, 556–563, Apr. 1990.

[42] Montgomery, J. P., and K. R. Davey, "The solution of planar periodic structures using iterative methods," *Electromagnetics*, **5, 2-3**, 209–235, 1985.

[43] Kastner, R., and N. Herscovici, "A Concise Conjugate Gradient Computation of Plate Problems with Many Excitations," 1989 APS/URSI Symposium, San Jose, CA.

[44] Jin, J. M., and J. L. Volakis, "TM scattering by an inhomogeneous filled aperture in a thick conducting plane," *IEE Proceeding–H*, **137**, 153–159, June 1990.

[45] Collins, J. D., J. L. Volakis, and J. M. Jin, "A combined finite element–boundary integral formulation for solution of two–dimensional scattering problems via CGFFT," *IEEE Trans. Antennas Propagat.*, Nov. 1990.